ANALYSIS OF DENSE 3D SEISMIC DATA AROUND THE SCROVEGNI CHAPEL IN PADUA, ITALY

Università degli Studi di Padova

Department of Geosciences

Geophysics for Natural Risks and Resources (L-79)

Candidate:

JOHN TING TIEW FUONG

Supervisors:

Dr. Ilaria Barone

Dr. Mirko Pavoni

Table of Contents

Abstract ……..…..(3)

1. Introduction …….……...(3)
2. Seismic waves……..……(4)
   2.1 Body waves…….…...(5-6)
   2.2 Surface waves…….……(6-8)
3. Seismic methods…….…….(9)
   3.1 Seismic Refraction…….…..(9-13)
   3.2 Surface waves Analysis……...…(13-15)
4. Materials and methods……..... (16)
   4.1 Acquisition setup……....(16-18)
   4.2 Seismic refraction tomography……..……..(18)
      4.2.1 First Break Picking……...…...(18-22)
      4.2.2 2D Synthetic Initial Model and Refraction Tomography……...….(22-27)
      4.2.3 2D Refraction Tomography for Field Data……..…...(27-29)
      4.2.4 Pseudo-3D Synthetic Initial Model and 3D Refraction Tomography……..(29-36)
      4.2.5 3D Refraction Tomography for Field Data……(37)
   4.3 Seismic surface wave tomography……..……(38)
      4.3.1 Preliminary Analysis……...….(38-41)
      4.3.2 Eikonal Tomography (Phase Velocity Maps) and Auto-Spectrum Gradient Computation……(41-45)
5. Results……...(46)
      5.1 2D Inverted model for field data……....(46-47)
      5.2 3D Inverted model for field data……....(47-51)
      5.3 Auto-spectrum gradient maps and Phase Velocity maps……...(51-56)
6. Discussion……(57-59)
7. Conclusion…….. (59)

References ……...(59-60)

Acknowledgement…….(60)

Abstract

In this thesis, a comprehensive 3D seismic survey was conducted in the vicinity of the Scrovegni Chapel in Padua, Italy, utilizing a combination of surface wave analysis and 3D refraction tomography. The survey used 188 nodes strategically positioned around the Scrovegni Chapel, and 28 active shots were fired within the survey area. The analysis focused on extracting travel times from the phases of the signal to analyse the fundamental mode of surface waves, specifically Rayleigh waves. Eikonal Tomography was employed to generate phase velocity maps, while the amplitude of the surface waves was examined to produce auto-spectrum gradient maps. The Geogiga software is used to produce the 3D refraction tomography.

Given the particulars of 3D refraction tomography, a preliminary exploration involved 2D initial model and 2D refraction tomography to fine-tune the parameters crucial for the subsequent 3D refraction tomography. The collaborative examination of surface wave analysis and 3D refraction tomography enabled the identification of noteworthy features, including two Roman walls and buried remnants of World War II structures. This collaborative approach underscores its utility for future shallow surveys.

1.0 Introduction

The Scrovegni Chapel, dedicated to Santa Maria della Carità and renowned for its exceptional cycle of paintings by Giotto, holds cultural significance. The frescoed cycle within the chapel was recognized for its cultural and historical importance, leading to its inclusion on the UNESCO World Heritage List in 2021. This recognition is part of the larger serial site known as "The frescoed cycles of the 14th century in Padua, Italy."

The Scrovegni Chapel is placed atop the remnants of a Roman amphitheatre, featuring distinct levels—one at the surface and another below ground, known as the hypogeum, as detailed in the study by Barone et al., 2022. Numerous archaeological and seismic surveys have been conducted in this location to unravel the significance of the hypogeum within the chapel and its connection to concealed remnants of the Roman amphitheatre. The complex nature of this site, coupled with limited available elements, has resulted in challenges, leaving a considerable portion of undiscovered remains yet to be explored.

The objective of this study is to enhance our understanding of the region through shallow survey methods, aiming to discover buried remains. Additionally, the study seeks to validate the efficacy of a joint analysis approach, integrating surface wave analysis and 3D refraction tomography, as a valuable tool for shallow surveying in this context. To achieve this goal, the study uses surface wave analysis, extracting travel times from signals and generating auto-spectrum gradient maps and phase velocity maps to identify anomalies. This methodology, previously applied by Barone et al. in 2022 to small-scale near-surface data, is chosen for its ability to resolve lateral velocity variations. Moreover, 3D refraction tomography is concurrently conducted to validate the findings derived from both surface wave analysis and 3D refraction tomography. Specifically, Geogiga software is employed for the inversion process of 3D refraction tomography.

In this study, we conduct a 3D dense nodes seismic survey primarily to analyse the propagation of Rayleigh waves. Specifically, the active seismic data obtained from the 3D dataset is utilized for both 3D refraction tomography and the generation of phase velocity and auto-spectrum maps.

2. Seismic waves

Seismic waves can be generated through natural processes or human activities (anthropogenic). The most prevalent natural source of seismic waves is tectonic activity, often associated with earthquakes. Earthquakes occur due to the sudden release of accumulated stress, typically along fault or plate boundaries (Bormann et al., 2012). This stress release results in the generation of seismic waves. These waves then propagate through or along the Earth's surface, resulting in ground shaking. Although a large number of weak tectonic earthquakes occur annually on a global scale, the majority of these events are of such low magnitude that their detection requires the use of highly sensitive instruments positioned in proximity to the seismic source. Earthquakes of significant magnitude, those equal to or greater than 6 on the Richter scale, occur less frequently; however, their occurrence has the potential to lead to extensive and devastating disasters (Bormann et al., 2012).

Seismic waves can also human-induced for exploration purposes. Explosions and weight-drop are the most commonly encountered sources. The primary distinction between seismic waves generated by earthquakes and those produced by explosions lies in their characteristics. Explosions typically generate a stronger uniform compressional motion (P-waves) that radiates in all directions, which is often more prominent than shear motion (S-waves). In contrast, earthquakes generate predominantly S-waves with varying amplitudes and polarities in multiple directions due to the complex and multidirectional ground motion (Hayes et al., 2017). In terms of duration, explosions produce impulsive signals with a very short period of seismic generation, whereas earthquakes typically generate signals with longer periods (Bormann et al., 2012). Earthquakes exhibit a broad frequency range, with a predominant concentration in the range of 0.01 to 10 Hz. However, they can also generate higher-frequency components, particularly in the case of smaller magnitude earthquakes (Tosi, 2012). Explosions, such as those associated with industrial or mining activities, generally generate seismic signals characterized by higher frequencies, frequently surpassing 10 Hz. Another anthropogenic source of seismic waves is weight-drop, which is also the source used for the data analysed of this thesis. The weight-drop method is typically employed for near-surface surveys, as it generates high-frequency signals primarily concentrated in the range exceeding 50 Hz. The weight-drop method generates seismic waves by releasing a mass from a specific height, which transfers energy to the ground and subsequently propagates through the Earth's subsurface. The frequencies produced by weight drops are typically lower than those generated by explosions and are often observed in the range between 5 to 60 Hz, with variations depending on the specific setup and parameters, including the mass of the weight used and the release height (Schwardt et al., 2022). Waves are characterized by a disturbance in a medium that carries energy and propagates. Importantly, the material through which the wave travels typically does not move with the wave. Instead, the motion of the material is generally limited to the displacement of small particles, known as particle motion. Once the wave passes through, these particles return to their original positions (Saleh, 2011). Seismic waves consist of body waves and surface waves. Body waves tend to propagate through the interior of the medium while surface waves tend to propagate along the surface of the medium. For this reason, body waves usually provide important information about the constitution of the interior of the Earth, meanwhile surface waves only sample the shallow Earth layers. Surface waves generally have higher amplitudes on the seismograms and contribute to the damage effects during earthquakes. In terms of frequency, body waves typically exhibit higher frequencies compared to surface waves.

2.1 Body waves

Body waves can be differentiated based on travel time. Primary waves (P-waves) travel faster than Secondary waves (S-waves) or Shear waves (Novotny, 1999). The P-waves are longitudinal waves (compressional waves) that can travel through both liquid and solid media and the motion is parallel to the direction of the wave propagation. Conversely, S-waves are transverse waves that can only travel through solid media and the motion is perpendicular to the direction of the wave propagation as shown in Figure 1. P-waves alter the volume of materials by cyclically compressing and expanding them as seismic waves pass through. On the other hand, S-waves change the shape of materials by displacing particles side to side.

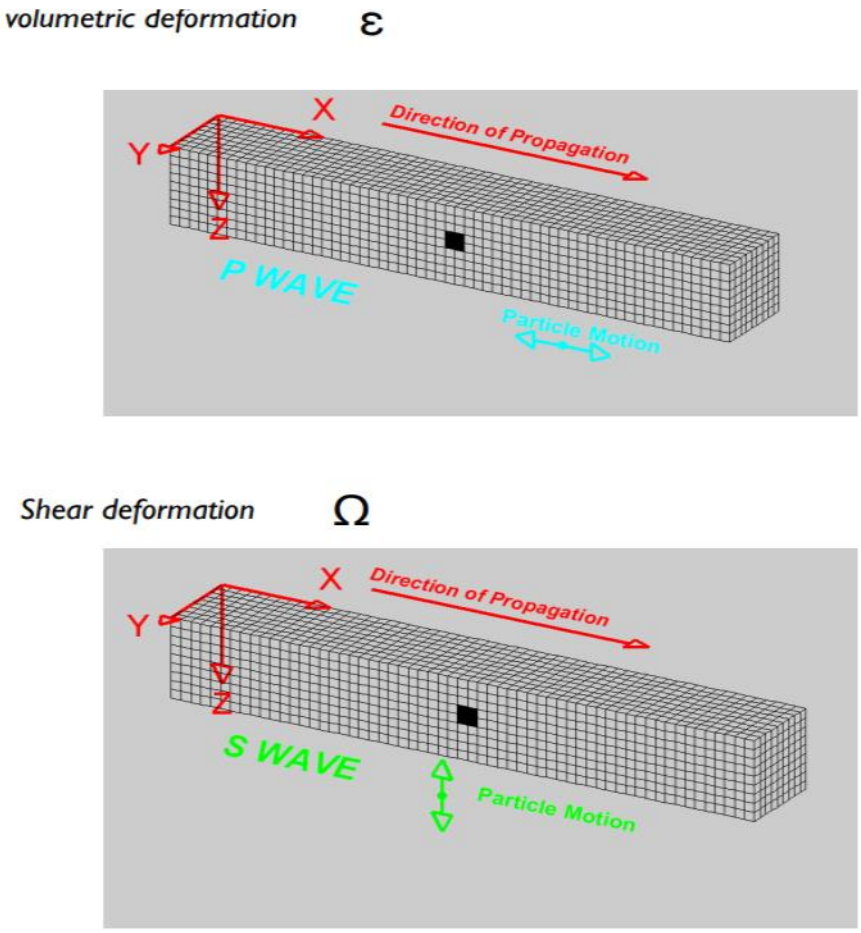

Figure 1: Wave propagation of P-wave and S-wave and the motion of the particles. Boaga, J. (2021)

Regarding velocity, the properties of seismic waves propagating in isotropic solid mediums are characterized by their wavelength (λ), frequency (f), and velocity (c). The wavelength of a seismic wave is directly proportional to its velocity and inversely proportional to its frequency. The phase velocity of seismic waves is mathematically expressed in Equation 1, where ω represents the angular frequency ($\omega = 2\pi f$) and k represents the wavenumber ($k = \lambda/2\pi$)

$$C = \frac{\omega}{k} \quad (1)$$

The speed of seismic wave propagation depends on several factors, including the composition of the rocks, temperature, and pressure. In general, different rock types can have varying velocities, but there are cases where specific rock types share the same velocity. Therefore, it is valuable to consider the

influence of temperature and pressure to understand these variations.
Temperature has a tendency to reduce the velocity of seismic waves, while pressure tends to increase their velocity. The relationship between temperature and seismic wave velocity is due to the thermal expansion of rocks at higher temperatures, which leads to decreased rock density and, in turn, reduces the speed of seismic wave travel. Conversely, higher pressure results in compaction, increasing the density of rocks and thereby enhancing seismic wave velocity.

The velocity of P-waves is associated with the elastic properties of materials, including Lame's constant (λ) for compressibility, shear modulus (μ), and the density (ρ) of the medium while the S-waves are only related to shear modulus (μ) and density (ρ) without Lame's constant as shown in the Equation 2.

$$Vp = \sqrt{\frac{(\lambda+2\mu)}{\rho}}$$

$$Vs = \sqrt{\frac{\mu}{\rho}} \qquad (2)$$

2.2 Surface Waves

Surface waves can be differentiated based on the motion and the interaction between the earth's surface as shown in Figure 2. There are two types of surface waves which are Love waves and Rayleigh waves. Rayleigh waves create an elliptical motion in which particles move in elliptical paths, influenced by a combination of both vertical and horizontal components. Meanwhile Love waves create a horizontal motion that is perpendicular to the direction of wave propagation. Love waves are typically faster than Rayleigh waves due to the motion of propagation. Both types of surface waves have a much slower decay rate compare to body waves due to the geometric spreading. Geometric spreading consists in the decay of energy of seismic waves based on the distance from the source (Fjær.E et al., 2021). In terms of decay rate, surface waves decay with 1/r, where r is the distance from the source, while body waves decay with $1/r^2$. This is because the surface waves propagate on the Earth's surface with cylindrical wavefront meanwhile body waves propagate through the earth's interior with hemispherical wavefront.

Rayleigh waves exist across a wide range of frequencies. In the field of geophysics, Rayleigh waves typically span frequencies ranging from 0.05 Hz to 10 Hz, making them valuable for seismic surveys. Rayleigh waves occur on the free boundary of a solid medium, meaning they are found at the interface between a solid and another medium. This other medium is typically either a vacuum or, in certain cases, an atmospheric gas if the density of the atmospheric gas is significantly lower than that of the solid medium. For Rayleigh waves to be considered, the solid medium must be an elastic isotropic medium. Elasticity implies that the material can deform under stress and return to its original shape when the stress is released. Isotropic means that the material's properties are the same in all directions. These conditions are necessary to enable the propagation of Rayleigh waves in the material.

Love waves, a type of shear horizontal (SH) surface waves require specific conditions to exist. They typically propagate in a surface waveguide, which consists of a surface layer rigidly bonded to an elastic substrate as shown in Figure 3. A fundamental requirement for the existence of Love waves is the presence of an elastic surface layer. This layer is typically situated at the top of the Earth's surface and plays a crucial role in supporting the propagation of these waves. Moreover, the elastic surface layer must exhibit a lower phase velocity than the underlying elastic substrate. The phase velocity of

Love waves is directly linked to the properties of these two layers, with the surface layer being characterized as having a "slower" phase velocity compared to the substrate.

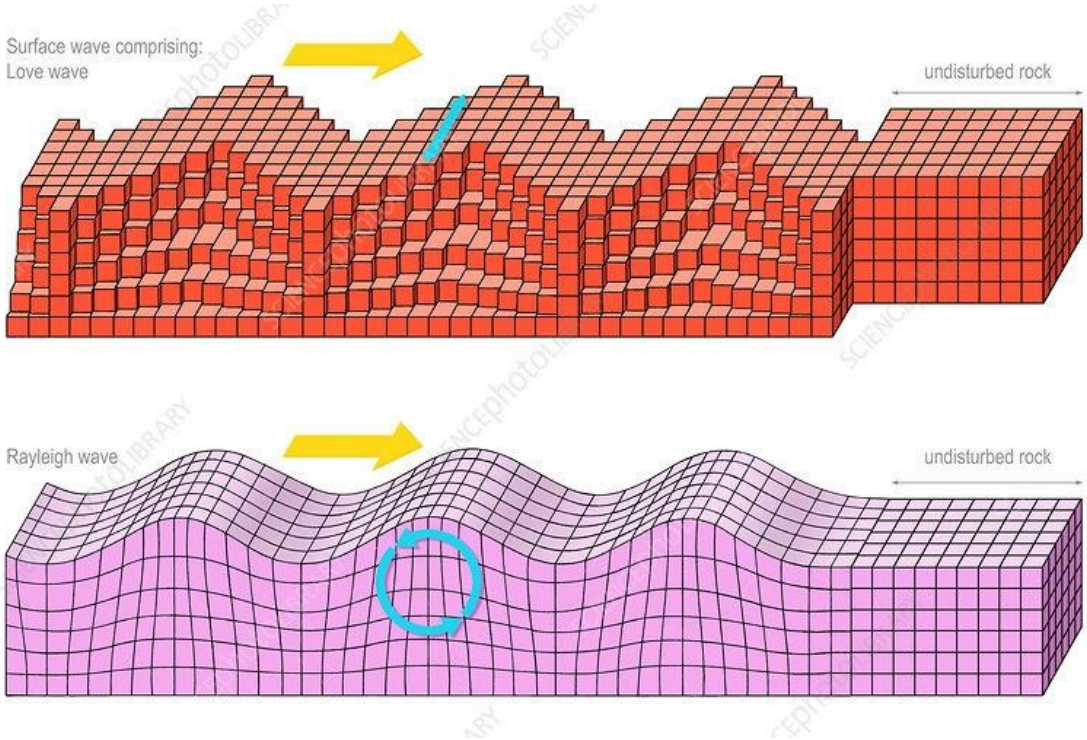

Figure 2: Wave propagation of Love wave and Surface wave with the particle motion. Hincks, G. (no date)

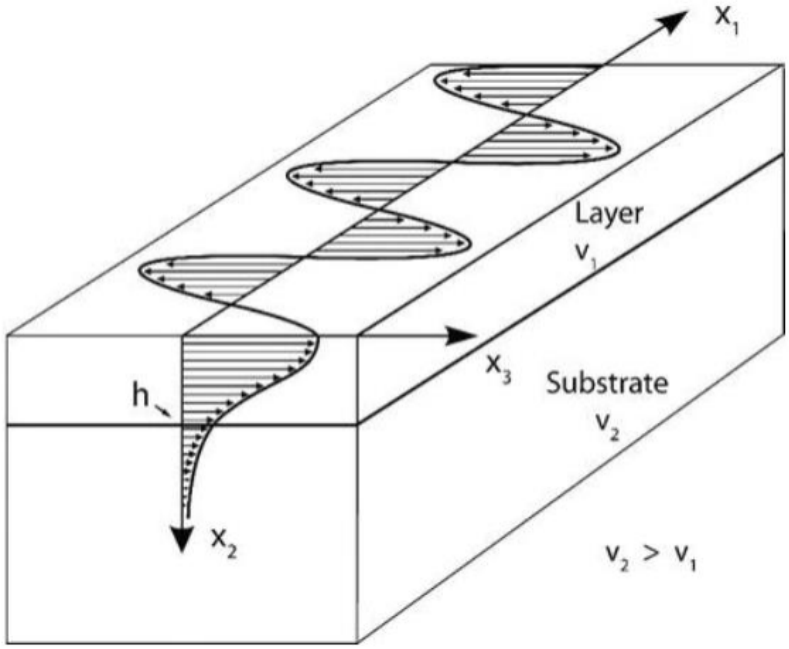

Figure 3: Wave propagation of Love Wave with different layers. Boaga, J. (2021)

Dispersion is a vital aspect of seismic waves, referring to the phenomenon in which the velocity of seismic waves varies with their frequencies. Various frequency components of seismic waves can travel at different velocities, resulting in the dispersion of the waves over time. Surface waves can exhibit both dispersive and non-dispersive behaviours. However, it is exceedingly rare for surface waves to demonstrate non-dispersive characteristics due to velocities generally increasing with depth. When surface waves propagate along the Earth's surface with varying frequencies, they frequently display dispersive behaviour (Zhang et al., 2023). Rayleigh waves typically exhibit more dispersion than Love waves due to the interaction between the shear and compressional components and its elliptical motion (Ying et al., 2014).

The wave sequence generated by surface waves can be constructed by summing the contributions of various modes. These modes represent different components of ground motion, as illustrated in Figure 4. The fundamental mode is the simplest mode, characterized by the lowest frequency oscillations. As the mode number increases, the frequency also increases, leading to higher-frequency oscillations. Each mode possesses a unique sensitivity to various depths within the subsurface. The fundamental mode prevails at shallow depths because of its characteristic motion pattern, which involves simple and large-scale motion, along with its energy distribution. In contrast, higher modes extend deeper into the subsurface because of their more complex motion patterns, which include a greater number of oscillations. These complex motions can interact more with the deeper subsurface medium, allowing them to probe deeper depths. Hence, during seismic recording, the fundamental mode typically arrives earlier on seismograms and dominates the initial phases of recorded signals.

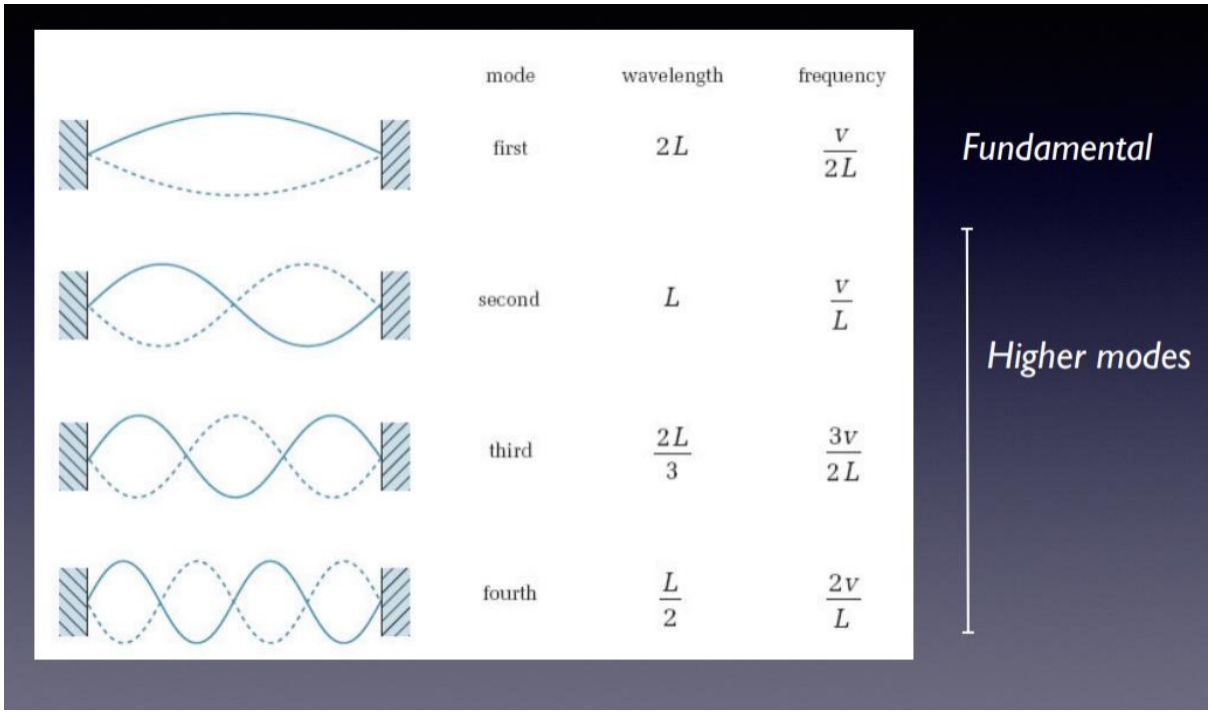

Figure 4: Various mode of surface wave propagation. Boaga, J. (2021)

3.0 Seismic methods

Seismic methods have been long used in geophysics field to image the subsurface structures and the geological formations (Bruno, 2023). These include seismic reflection, seismic refraction and surface wave analysis. The properties of the structure and ground (elasticity, stiffness and density) can be retrieved by studying the propagation of seismic waves. Generally, seismic methods involve a source that generates the seismic waves (either naturally occurring or user-generated), a series of receivers (geophones) and an instrument (seismograph) for recording the seismic waves motion. These data would help to detect the subsurface objects and identify the velocity variations in depth. The thesis will primarily concentrate on seismic refraction and surface wave analysis.

3.1 Seismic Refraction

A critical parameter to consider during refraction surveys is acoustic impedance, which serves as a fundamental descriptor of a material's efficiency in transmitting acoustic waves. It is calculated as the product of the structure's density and the speed of sound within the structure ($I = \rho V$). When seismic waves encounter an interface between two mediums with different acoustic impedances, part of the wave energy is reflected back into the first medium, part is refracted into the second medium, and part of the wave energy is also absorbed by the interface. The transmitted energy is dependent on the acoustic impedance difference and the variation in acoustic impedance helps to image the structures of subsurface. The acoustic impedance contrast between two mediums can be calculated using the Equation 3.

$$R=\frac{I2-I1}{I2+I1}=\frac{\rho 2V2-\rho 1V1}{\rho 2V2+\rho 1V1} \quad (3)$$

Seismic refraction is based on the principle of Snell's law which describes the refraction of seismic waves when they pass through different sub-surface layers with different velocities of propagation. The law is expressed in Equation 4, where V1 and V2 represent the velocities in the first medium and in the second medium respectively, $\theta 1$ denotes the angle of incidence and $\theta 2$ denotes the angle refraction.

$$\frac{\sin\theta 1}{\sin\theta 2}=\frac{V1}{V2} \quad (4)$$

Equation 4 defines that, when a seismic wave crosses the boundary between two media with different velocities of propagation (V1 and V2), the ratio between the sine of the angles $\theta 1$ and $\theta 2$ is constant and equal to the ratio between V1 and V2. When $\theta 2$ is equal to 90°, the refracted waves propagate along the boundary interface of the media, and in this situation the value of $\theta 1$ is referred as the critical angle. While the refracted wave travels along the boundary, it generates secondary wave fronts (as expressed by Huygens' Principle), which emerge at the surface, as shown in in Figure 5. The equation for this particular scenario is expressed in Equation 5.

$$i_c = sin^{-1}(\frac{V1}{V2}) \quad (5)$$

where i_c represents the critical angle of refraction.

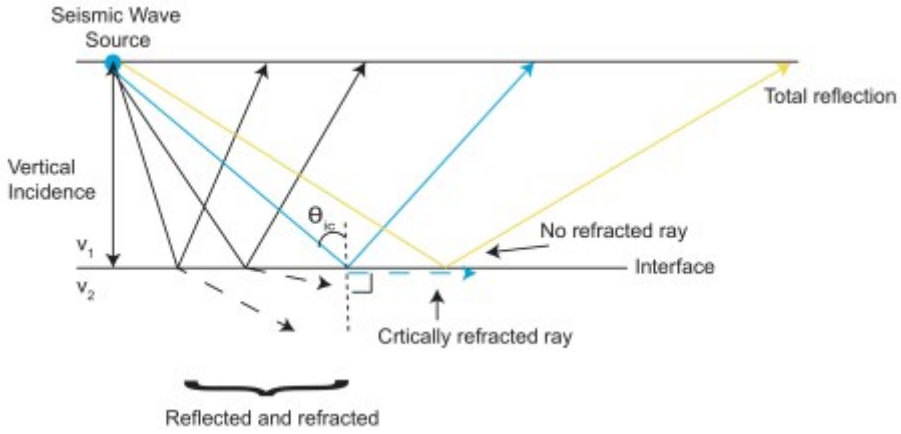

Figure 5 : Wave refraction and the critical refraction. Billen, M. (no date)

In conclusion, seismic wave refraction occurs when a an interface between two subsurface layers with different seismic velocity propagations.

The recorded signals typically include both direct waves and refracted waves as the first arrival waves. The direct waves travel horizontally along the surface and can be calculated using the equation 6.

$$T = \frac{x}{V_1} \qquad (6)$$

The direct ray arrival time, represented by the slope (m) of $\frac{1}{V_1}$ and the intercept of 0, can be obtained through the equation above. By obtaining the first arrival time, the plot of travel time versus the distance can be generated, as shown in Figure 6. Consequently, the velocity of the V1 can be derived using $\frac{1}{m}$

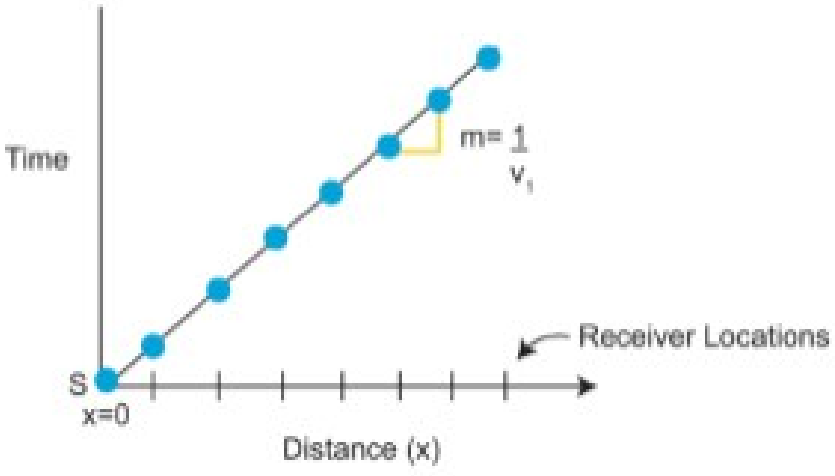

Figure 6: Time versus distance plot. Billen, M. (no date)

Moreover, the time for the seismic wave to reach the receivers can be calculated using the Equation 7, where h in the equation represents the thickness of the layer.

$$T = \frac{2h}{V_1} \qquad (7)$$

To obtain the travel time for refracted waves, as shown in Figure 7, Equation 8 is used.

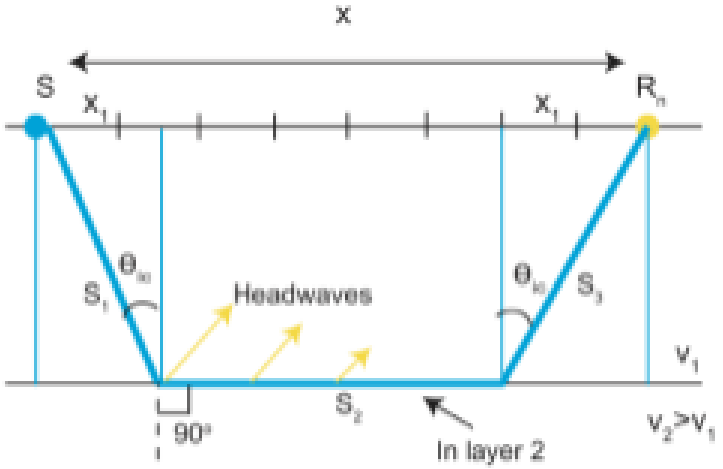

Figure 7: Refracted waves (Head waves). Billen, M. (no date)

$$T = T1 + T2 + T3 = \frac{S_1}{V_1} + \frac{S_2}{V_2} + \frac{S_2}{V_3} \qquad (8)$$

Since S1 is equal to S3 so the equation X can be derived into equation 9.

$$T = \frac{2S_1}{V_1} + S_2 \qquad (9)$$

The first arrival time can then be derived as shown in Equation 10.

$$T = \frac{x}{V_2} + \frac{2h\,(V_2^2 - V_1^2)^{\frac{1}{2}}}{V_1 V_2} \qquad (10)$$

With this equation, the slope of the refracted wave would be m = $\frac{1}{V_2}$ with the intercept of $\frac{2h\,(V_2^2 - V_1^2)^{\frac{1}{2}}}{V_1 V_2}$

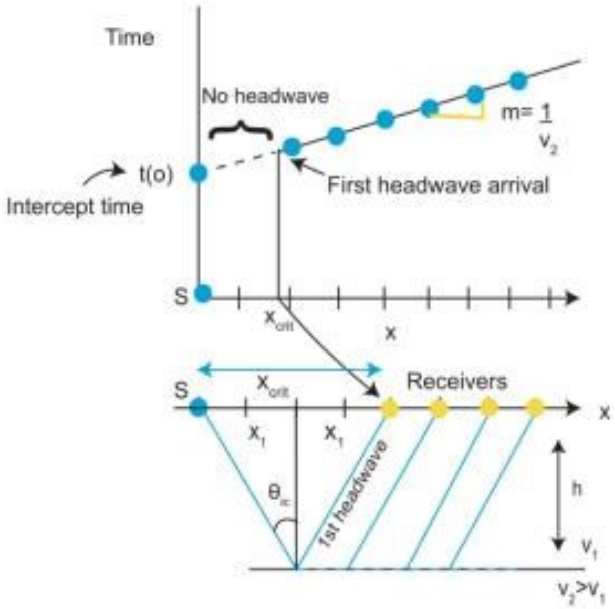

Figure 8: Time versus Distance plot for refracted wave and crossover distance (Xc). Billen, M. (no date)

Figure 8 illustrates the refracted wave plot, emphasizing the significance of the crossover distance (Xc). The Xc represents the distance at which the first arrival times of both the direct wave and refracted wave coincide. Prior to reaching the Xc, the direct wave arrives first, while beyond the Xc, the refracted wave arrive first, as shown in Figure 9. Using the intercept time and the velocity of the second layer, the thickness of the layer can be subsequently calculated.

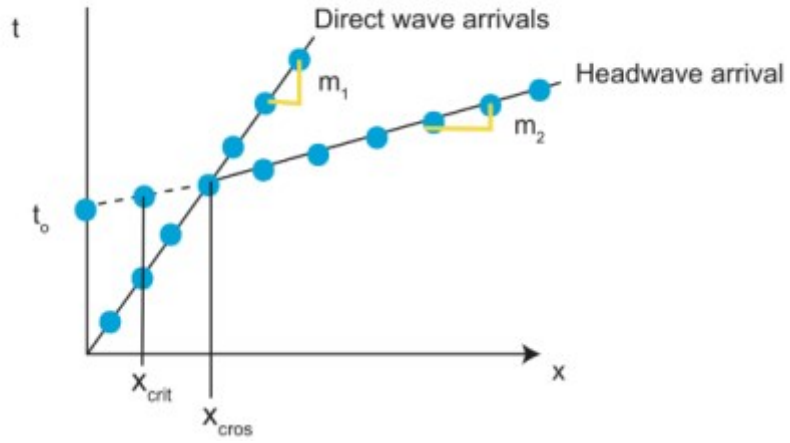

Figure 9: Direct wave and head wave arrival times

Figure 9 shows the arrival time difference between the direct wave and refracted wave. Through careful analysis of the plot, it is possible to derive the thickness and travel time for two distinct layers. Additionally, it is essential to highlight that in cases where V1 exceeds V2, no head waves are generated, leading to the absence of refraction.

The seismic refraction method allows the retrieval of a Vp (compressional wave velocity) model. The initial step in obtaining the Vp model involves first-break picking. First-break picking in seismic refraction entails identifying and selecting the arrival time of the first seismic wave that reaches the geophones or receivers in a refraction seismic survey. The "first break," which corresponds to the

initial arrival time, is typically attributed to the direct P-wave (compressional wave) and refracted waves arrival from the seismic source. Following the first-break picking, a travel-time tomography is carried out to acquire the P-wave velocity in the near-surface.

First-arrival travel times are selected for each trace, and the tomography algorithm proceeds by iteratively refining the near-surface velocity model. This refinement is achieved by minimizing a misfit function that quantifies the disparity between the observed travel times and the modelled travel times. Selecting the first-arrival travel times can be a challenging task, as they may be affected by noise in the input data. To mitigate the influence of noise, a misfit function is typically employed to minimize the discrepancies between observed and modelled travel times. Further methodological details will be addressed in the subsequent chapter.

3.2 Surface Wave Analysis

Surface wave analysis is a method that primarily focuses on the study of surface waves that travel along the Earth's surface without significant penetration into the Earth's subsurface.
The objective of surface wave analysis is to construct a Vs (shear wave velocity) model of the Earth's subsurface. The initial stage in deriving a Vs model through surface wave analysis involves collecting seismic data using an array of ground-based geophones and a seismic source. The seismic data is subsequently subjected to a data processing phase to estimate the dispersion curve, followed by an inversion process to derive the Vs (shear wave velocity) model.

Dispersion is intricately linked to the phase velocities of surface waves, as distinct frequencies with different wavelengths of surface waves propagate at varying phase velocities. Hence, through an analysis of the phase velocity and the dispersion characteristics of surface waves, we can derive a dispersion curve. A dispersion curve serves as a graphical tool for the analysis of the dispersive characteristics exhibited by surface waves, aiding in the identification of their fundamental modes (Foti et al., 2000). Let's consider a stratified medium, as illustrated in Figure 10a, with increasing stiffness resulting in an increase in shear-wave velocity with depth. In this scenario, the high-frequency Rayleigh wave (short wavelength), as illustrated in Figure 10b**,** traveling in the top layer will exhibit a propagation velocity slightly lower than the shear wave in the first layer. Conversely, the low-frequency surface wave will propagate at a higher velocity as it encounters the stiffer underlying medium, as depicted in Figure 10c. This concept can be extended to encompass various frequency components. Figure 10d depicts a phase velocity versus wavelength plot, indicating an increasing trend for longer wavelengths. As mentioned earlier, wavelength is closely tied to frequency. Therefore, this information can be represented in the form of a phase velocity versus frequency plot, as depicted in Figure 10e and is commonly referred to as a dispersion curve. This example illustrates that the dispersion curve is linked to the changes in medium parameters with depth within a vertically heterogeneous medium. In Figure 10, only the dispersion of the fundamental mode is depicted, but it should be noted that vertically heterogeneous media typically accommodate multiple modes of

surface wave propagation.

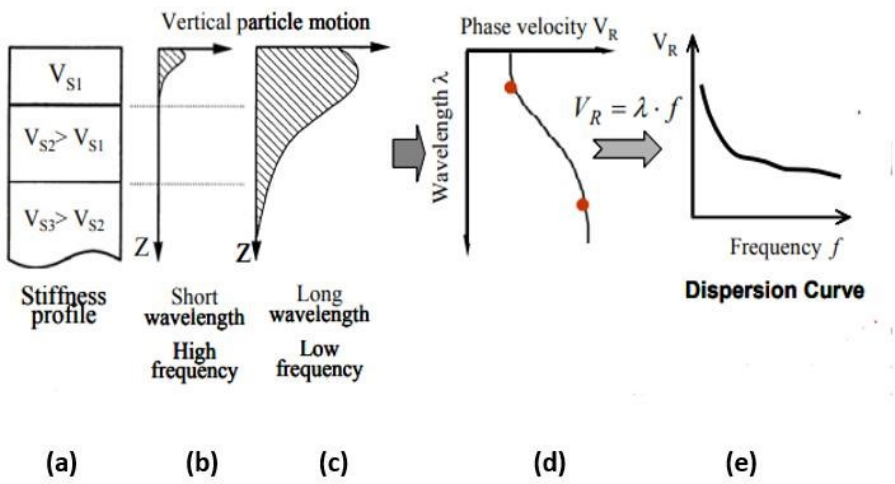

Figure 10(a): stiffness profile of layers. Figure 10(b) and Figure 10(c): Surface wave propagation at different frequencies. Figure 10(d): Phase velocity versus wavelength plot. Figure 10(e): Dispersion curve. Boaga, J. (2021)

Following the acquisition of the dispersion curve, an inversion process is performed to derive the Vs model, revealing the variation of shear wave velocities with depth as illustrated in Figure 11. In practice, the solution to the inverse problem involves selecting a set of model parameters that closely matches the numerical dispersion curve generated by the forward problem with the experimental dispersion curve of the site. In the context of surface wave analysis, the forward problem entails the use of a model with known parameters to predict and simulate data, specifically numerical dispersion curves. These curves represent the expected dispersion behaviours based on a defined set of model parameters. Conversely, the inverse problem in surface wave analysis involves the process of deducing model parameters from the observed data, which is typically the experimental dispersive curve representing actual measurements at the site. The goal of this process is to identify a set of parameters that closely match the observed data. When this goal is met, it suggests that the model parameters provide a reasonable representation of the subsurface properties at the site, and thus, the Vs model obtained is considered suitable.

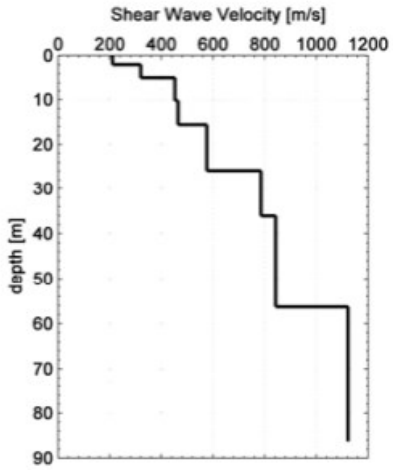

Figure 11 shows the plot of depth (m) vs shear wave velocity (m/s). Boaga, J. (2021)

Regarding the depth of penetration, it is determined by wavelength (λ), phase velocity (c), and frequency (f), as indicated in Equation 11.

$$\lambda = \frac{c}{f} \qquad (11)$$

Resolution is the ability to distinguish between two features that are very closely positioned, representing the minimum separation required to preserve their individual identities (Sheriff, 1997). In terms of seismic resolution, achieving optimal vertical and lateral resolution often requires striking a balance among various factors, including frequency, source type and receiver spacing. This balance is essential to meet the specific goals of the investigation. The seismic frequency content depends on the bandwidth of the signal, which generally decreases with depth due to the attenuation of seismic waves. Both horizontal and vertical resolution is determined by the wavelength of the seismic waves (λ), which in turn depends on the frequency and seismic velocities. The resolution decreases as you move deeper into the Earth because of lower frequencies and longer wavelengths.. Likewise, in terms of receiver spacing, the distance between geophones can influence lateral resolution, with closer spacing offering improved lateral resolution by densely sampling the subsurface. Increased spatial density of receivers facilitates the detection of higher-frequency components within the surface waves, which, in turn, provides more detailed information about subsurface structures and lateral velocity variations. Finally, the choice of source for generating surface waves can significantly impact the data quality, as employing high-energy sources generally results in improved resolution.

4.0 Materials and methods

In this section, the methods and materials employed in this thesis will be discussed, including the acquisition setup, the 3D refraction tomography, and the seismic surface wave analysis.

4.1 Acquisition setup

The acquisition setup for both seismic refraction and surface wave analysis remains consistent throughout this thesis. The seismic energy source utilized in this study involved a 70kg metallic disc descending from a height of 1.5 meters. This method, despite its tendency to generate low-frequency energy and relatively large amounts of coherent noise, holds historical significance as one of the earliest non-explosive sources to achieve widespread acceptance in seismic studies (Abe et al., 1990). Each location was energized at least twice to amplify the energy and enhance the signal-to-noise ratio. Total of 54 active shots were performed to produce a uniform azimuth distribution that allow the seismic waves to distribute evenly in all directions around the area of interest. A total of 188 seismic nodes were positioned at the surface around the Scrovegni Chapel, with uniform 3-meter spacing both in South-North and East-West direction. The grid was carefully planned to cover the area of interest surrounding the chapel, with the receiver spacing chosen to meet the necessary resolution for imaging that specific area. Seismic nodes are instrumental devices or receivers employed for the recording of seismic waves. They are equipped with velocimeters capable of measuring ground motion. The nodes have the capability to measure vertical and possibly horizontal velocity within a frequency range of 5-150 Hz depending of the seismometers used. The nodal system consists of 1C tripod, 1C spike and 3C as illustrated in Figure 12 and Figure 13.

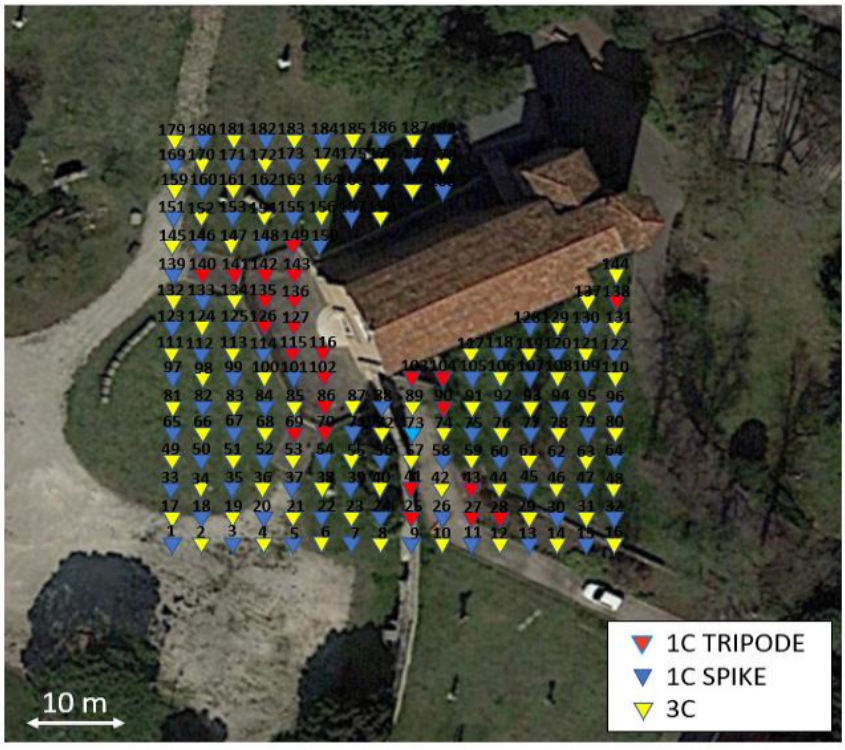

Figure 12 : Acquisition setup for analysis including the type of nodes used and the location.

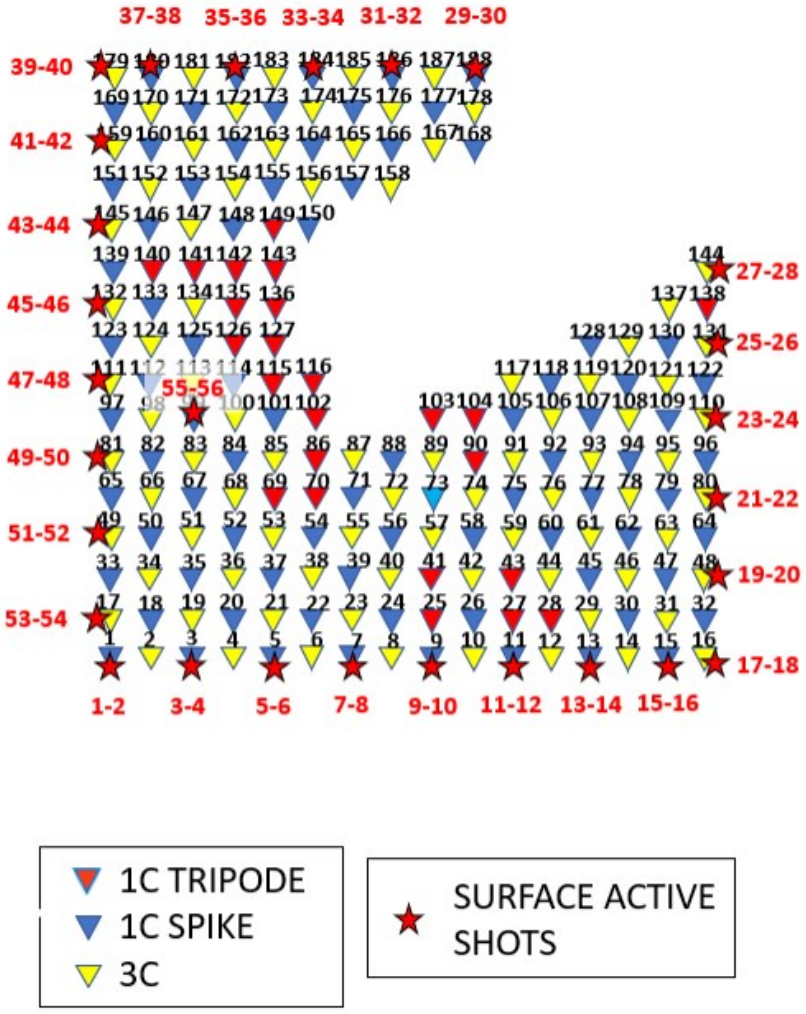

Figure 13: Nodes and sources location.

1C denotes the single-component geophones that record ground motion in a single direction, typically in the z-component, which corresponds to vertical ground movement (up and down). The difference between a 1C spike and a 1C tripod is that a 1C spike is attached to a spike that is typically inserted into the ground for stabilization and support, while a 1C tripod is affixed to a tripod, which is a three-legged stand. During the survey, a total of 105 1C receivers were deployed, with 1C tripods primarily used in areas such as roads and pavements where the ground is not easily penetrated by spikes. On the other hand, 83 sets of 3C sensors were also positioned between the 1C sensors to capture additional details for the analysis. Unlike the 1C geophones, 3C geophones have the ability to record the signal in three components, including the vertical (z-axis), South-North direction (y-axis), and East-West direction (x-axis) as illustrated in Figure 14. By combining the use of both 1C and 3C sensors, the survey would provide a more complete picture of the ground motion.

Figure 14: 1C spike on the left and the 3C on the right. SmartSolo, (no date)

Furthermore, seismic wave analysis is often affected by various sources of noise. In this survey, this noise refers to random ambient noise due to external factors such as roadside activities, given the survey location's proximity to a road. Consequently, filters will be used in the subsequent analysis to reduce the impact of noise on the recorded signals from the geophones.

4.2 Seismic Refraction tomography

The software used for seismic refraction tomography, both for the 2D and 3D approach, is GEOGIGA (Technology Corp.). The process for retrieve the Vp velocity model involves several key steps:

- First Break Picking
- 2D Synthetic Initial Model and Refraction Tomography
- 2D Refraction Tomography for Field Data
- Pseudo-3D Synthetic Initial Model and 3D Refraction Tomography
- 3D Refraction Tomography for field data

4.2.1 First Break Picking

First-break picking is a crucial initial step in seismic refraction surveys. For each shot position, it involves identifying the first-time arrivals of the P-waves at the receivers. While automatic picking by software is an option, this study involved manual picking of all the seismic traces to obtain more accurate and detailed results. Furthermore, the vicinity of the Scrovegni Chapel to the roadside introduced additional background noise during the seismic survey. The process of first-break picking is shown in Figure 15, outlining the workflow for this crucial step.

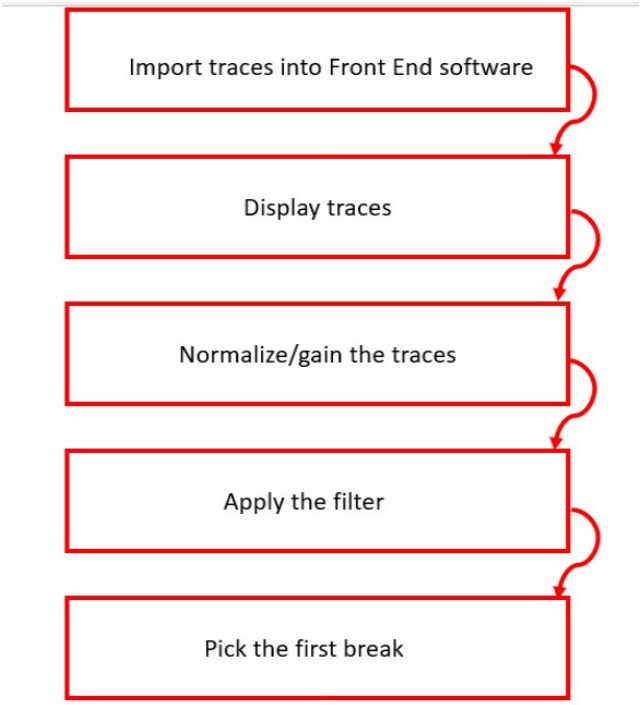

Figure 15 shows the workflow for the first break picking

Once the raw seismic record of a shot is displayed (e.g. Figure 16), to better identify the first-time arrival, the seismic traces can be adjusted using the normalize function that applies an amplitude normalization (e.g. Figure 17).

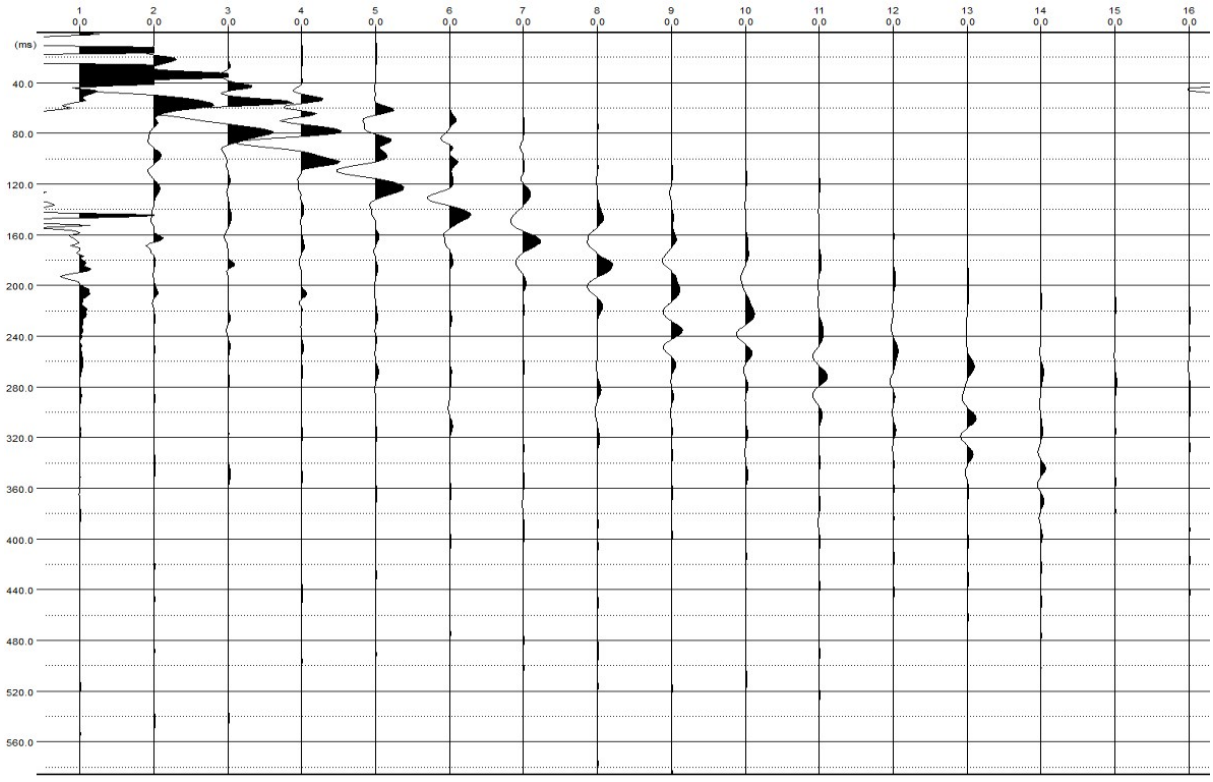

Figure 16: Example of active seismic record before normalization

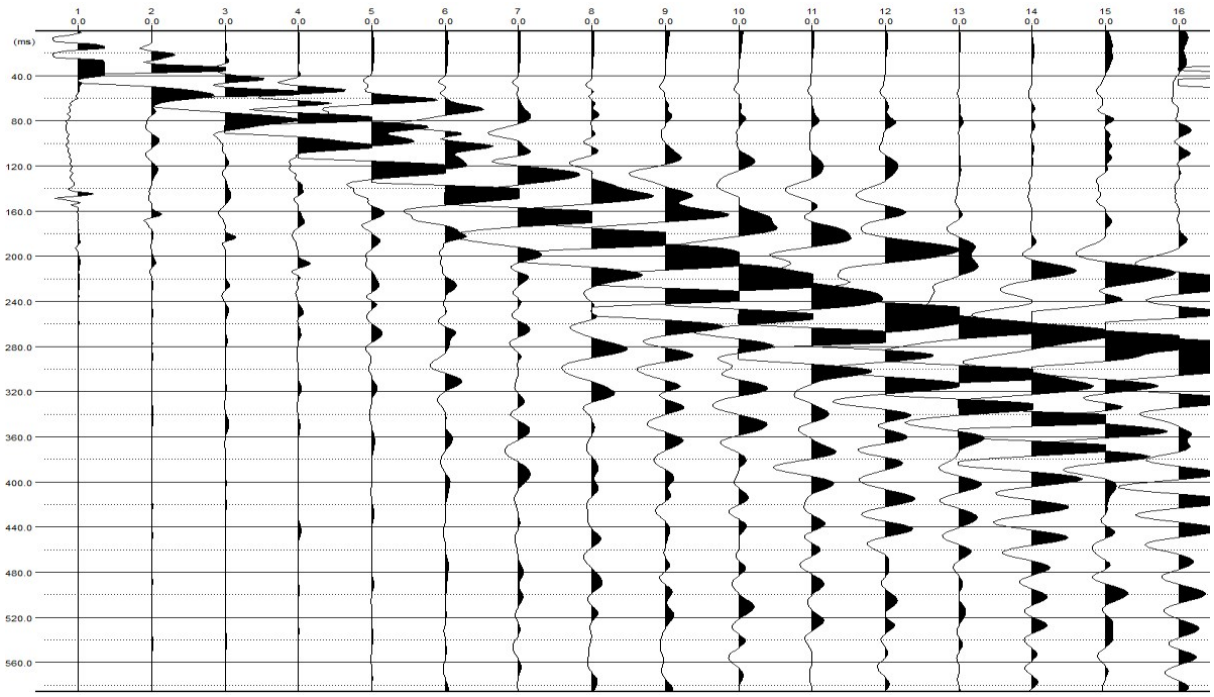

Figure 17: Normalization function applied to the seismic record shown in Figure 16.

As shown in Figure 17, there is a significant amount of unwanted noise in the seismic traces, which hinders the identification of the first-time arrivals. Nevertheless, seismic traces can be filtered using various types of filters, including band-pass, low-pass, high-pass (see Figure 18). A low-pass filter allows the transmission of signals containing frequency components below a specified cut-off frequency, while attenuating or blocking higher frequency components. On the other hand, a high-pass filter allows high-frequency components to pass through while attenuating low-frequency components. A notch filter, in contrast, attenuates a specific narrow range of frequencies while allowing other frequencies to pass through with minimal reduction.

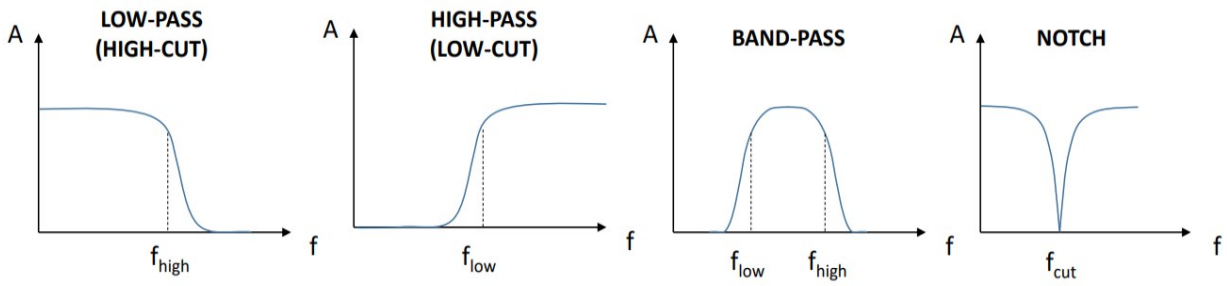

Figure 18 : Various types of filter. Barone, I. (2021)

In the presented analysis, we applied a band-pass filter, which requires two threshold frequencies: a lower cut-off frequency and an upper cut-off frequency. This filter is effective for isolating a specific frequency range within the seismic traces by defining the range or band of frequencies to pass through. The band-pass filters can have different tapers or filter shapes, but for this analysis, the Butterworth taper is the one used. A Butterworth taper is a specific type of window function used to smoothen the transition when a signal passes through a filter by reducing or tapering the abrupt changes at the edges of the signal. Figure 19 illustrates the band-pass filter applied in this process, featuring an upper cut-off frequency of 62.5 Hz and a lower cut-off frequency of 12.5 Hz.

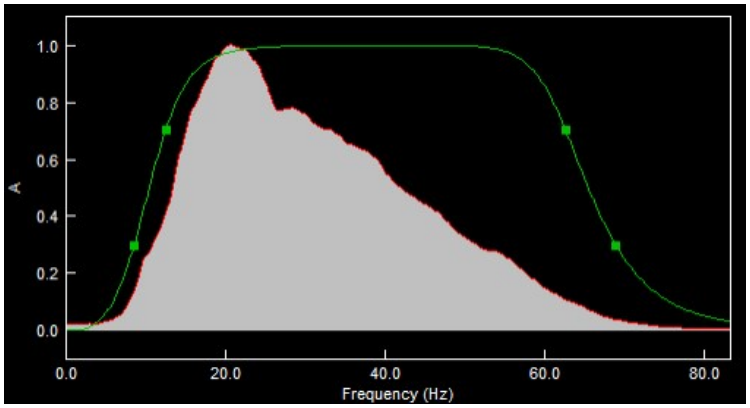

Figure 19: Band-pass filter applied

The band-pass filter proves highly valuable for the analysis in this survey partially eliminating the noise from the surrounding environment (e.g. Figure 20).

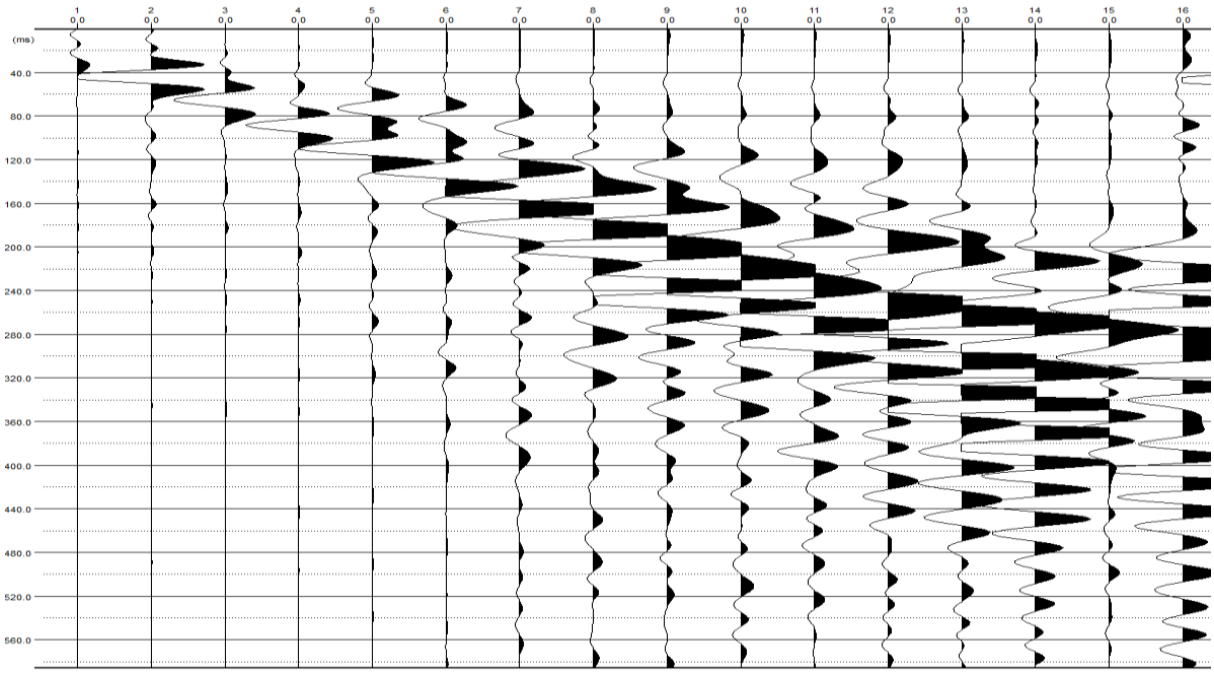

Figure 20: Result of the band-pass filtering applied to the seismic traces shown in Figure 17.

At this point, it was possible to apply a fairly reliable picking of the first-time arrivals (e.g. Figure 21)

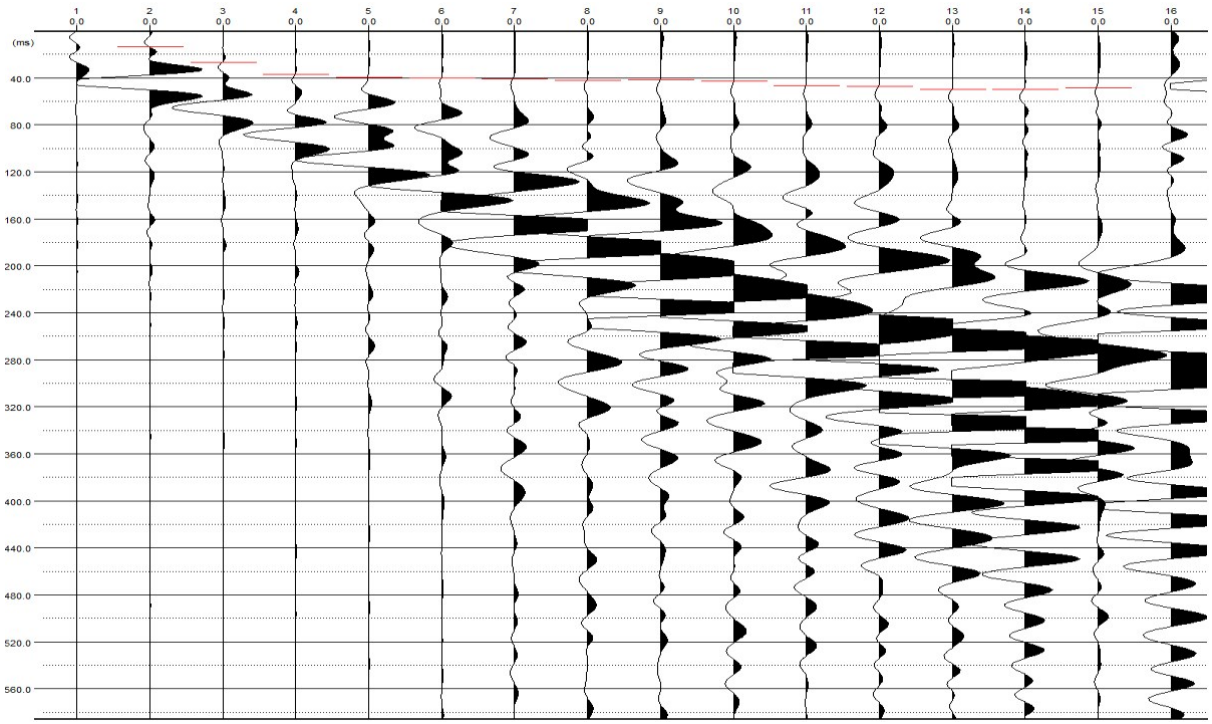

Figure 21: Picking of the first-time arrivals for the seismic record shown in Figure 18.

4.2.2 2D Synthetic Initial Model

A synthetic initial model is one that is artificially generated and not derived from actual data, serving as a starting point for the inversion process. An initial model has been created, featuring varying velocities for two subsurface layers and distinct velocities for the underlying wall. This model serve the purpose of identifying suitable parameters for the upcoming 2D inversion process. To construct the initial model, a velocity model must be defined. The survey area's geometry in the x-direction and z-direction is established for a complete understanding. In the x-direction geometry, the range extends from 0 to 48m with intervals of 0.5, capturing the spatial variation. Simultaneously, the initial model's depth is established at 10m, with intervals of 0.5 indicating the number of grid points used to represent the subsurface structure. The geometry is designed to align with the survey's geometry. Subsequently, a layered model is established, featuring a wall extending horizontally from 27.5m to 29.5m and reaching a depth of 5m. The wall has a P-wave velocity (Vp) of 1700 m/s, Shear velocity (Vs) of 1000 m/s and density (ρ) of 1700 kg/m^3. The first layer of this model has a thickness of 4m, a P-wave velocity (Vp) of 500 m/s, Shear velocity (Vs) of 300 m/s and a density (ρ) of 1300 kg/m^3. Following this, the second layer, representing the aquifer, has a thickness of 11m, a Vp of 1500 m/s, a Vs of 1000 m/s and a density (ρ) of 1500 kg/m^3.

The modelling setup involves strategically placing source positions at 3m, 9m, 15m, 21m, 27m, 33m, 39m, 45m, and 48m, comprising a total of 9 shots. The source positions in the x-direction are accurately aligned to correspond with the positions in the actual dataset. For receiver positions, a series spanning from 3m to 48m is established with a consistent 3m interval between each point. This arrangement results in a total of 16 channels, strategically positioned to capture a diverse range of seismic data. It is worth mentioning that the shot is deliberately positioned away from the wall to mitigate potential complexities in the seismic data. Figure 22 illustrates the spatial arrangement of both receivers and sources.

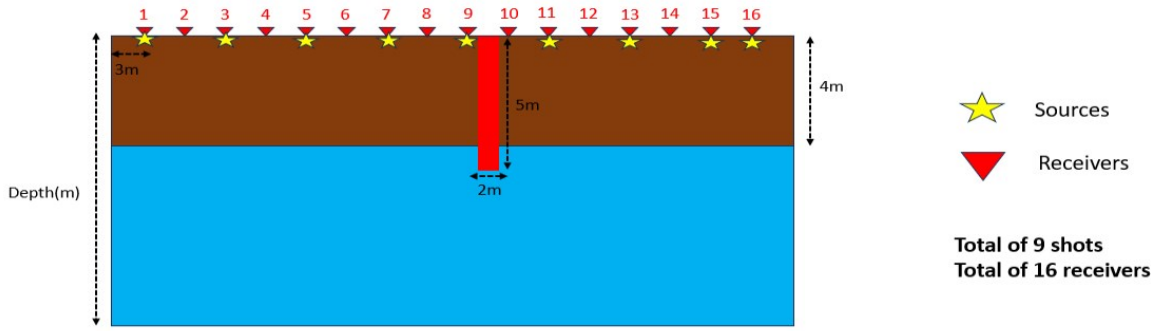

Figure 22: Sources and Receivers Position

Figure 23 show the outcomes of the initial model generated through the Geogiga 2D initial model software. These visual representations provide a snapshot of the subsurface characteristics and lay the foundation for subsequent inversion processes.

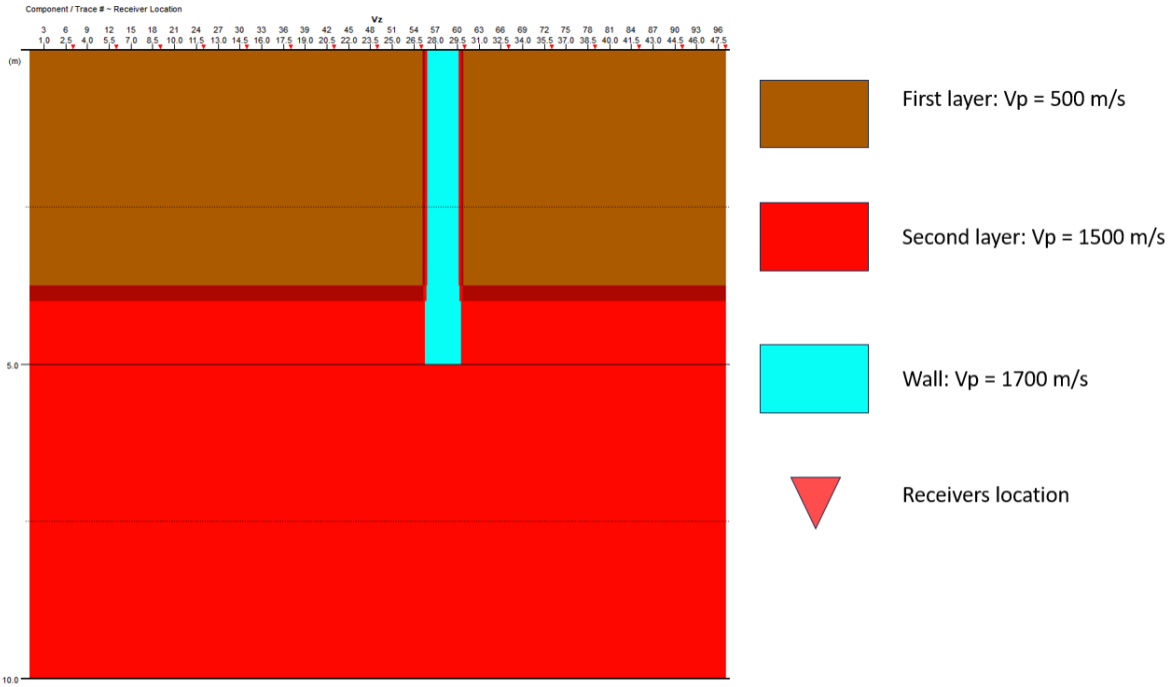

Figure 23: Initial Synthetic model generated through Geogiga 2D Initial model software

After setting up the modelling settings, seismic waves are generated, and the resulting travel times are recorded by the receivers. The recorded data is then saved as seismograms, and the first break picking process is conducted for subsequent use in 2D refraction tomography.

In 2D refraction tomography, the Travel-Time curve (TT curve) is constructed by integrating the first break picking data obtained from the seismic waves generated by the synthetic model with known parameters. This curve presents the travel times of seismic waves at various distances from the seismic source. In refraction tomography, an initial model is established by defining the initial model

parameters. Initially, the maximum inverted depth is set to 15m, consistent with the previously created synthetic model. The maximum offset of the array is also specified as 45m. Typically, the inverted depth is maintained at 1/3 to 1/6 of the maximum offset. This ensures a favourable resolution for depth considerations. A gradient model is then defined as the initial model, in which "gradient model" indicates a representation of the spatial variation of a specific property in respect to space—in this context, the property is velocity. The depth ranges from 0 to 15m, with velocity varying between 500 to 1700 m/s.

Several parameters need to be defined before initiating the inversion process, categorized into modelling and inversion parameters. For modelling, the shortest path ray tracing method is used. The subsurface is discretized into a grid of cells, and at each grid point, the algorithm calculates the shortest path of the ray from source to receivers. The default settings applied for horizontal and vertical spacing is defined as half of the receiver interval in the X-direction (dx), while the vertical spacing is set as ¼ of dx. These spacings correspond to the dimensions of the grid cells used for subsurface modelling. The spacings represent the distance between adjacent grid cells. In the current modelling configuration, a horizontal spacing of 0.4m and a vertical spacing of 0.5m are used. This means that the separation between adjacent grid cells is set to 0.4m in the x-direction and 0.5m in the vertical direction, facilitating a fine-grained representation of the subsurface structure.

Furthermore, the order for both horizontal and vertical directions must be defined. In the context of modelling settings, "order" refers to the complexity or degree of the model. In modelling, the order corresponds to the degree of the polynomial used to represent the relationship between variables. The order of a polynomial determines its flexibility in capturing different patterns, as higher-order polynomials have more terms with higher powers, providing increased flexibility to fit complex, non-linear patterns. In general, smaller spacing and higher order result in higher precision in modelling but require longer calculation times. Hence, finding the right balance between spacing and order is crucial to avoid oversimplification or overcomplication of the model. The default order setting is 4, but due to the complexity of the initial model, particularly the presence of a wall, the order is slightly increased to 6 for both horizontal and vertical directions to enhance the visualization of the wall.

In terms of inversion, the regularized inversion approach is used in refraction tomography. It includes some key parameters such as iteration, constraint, picking error and smoothing.

In the context of inversion processes, an iteration refers to one complete cycle of the algorithm used to update and refine the model parameters. The process starts with an initial model to simulate the observed data. Data misfit is then calculated by comparing the predicted data with the actual observed data to quantify the difference between them. The final model is created after a predefined number of iterations. The number of iterations needs to be chosen carefully, as too few iterations may result in underfitting and give a very simple inverted model. On the other hand, too many iterations may lead to overfitting, resulting in an overly complex model. The default setting for the maximum iteration is 5. However, when the inversion is carried out with only five iterations, the inverted model shows no changes in velocity variation with depth. This indicates that the maximum iteration is too low, leading to a failure in capturing any geological velocity variation. Therefore, after several trials and errors, the optimal setting for the iteration parameter in this inversion is 10. Figures 24 and 25 illustrate the comparison between two different numbers of iterations, 10 and 25, respectively. The inverted model with 10 iterations demonstrates a simpler model than the model with 25 iterations but yet capture the velocity variation of the wall. Additionally, a higher number of iterations results in a more complex structure compared to a lower number of iterations. This highlights that a higher number of iterations may not necessarily be beneficial even the misfit is reduced.

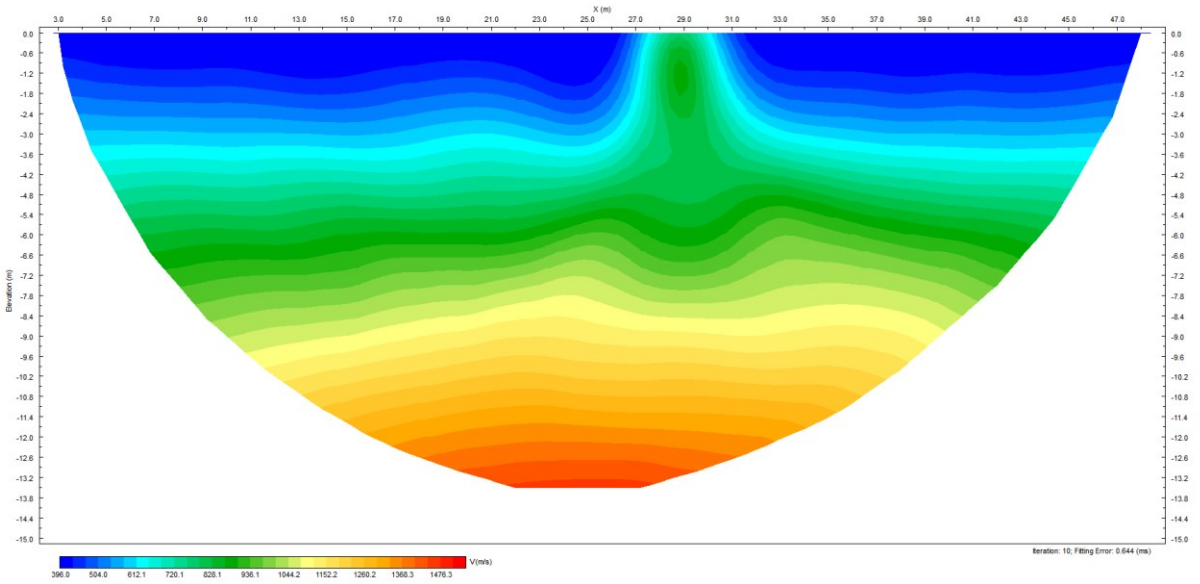

Figure 24: Inverted synthetic model with number of iterations of 10

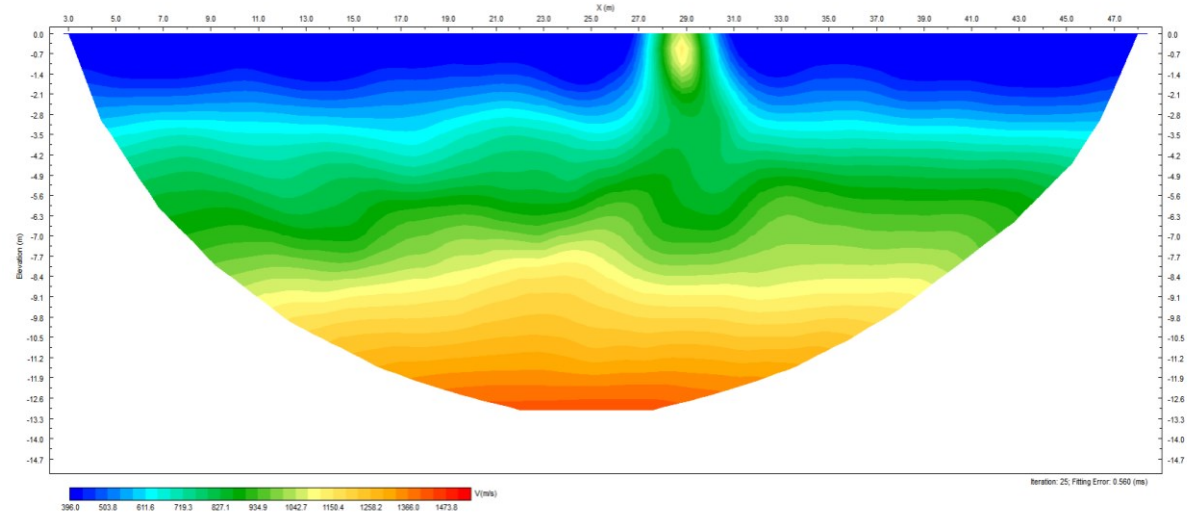

Figure 25: Inverted synthetic model with number of iterations of 25

The picking error is another crucial parameter in the inversion, as the precision of the first break picking determines the accuracy of the results. In this analysis, the first break picking is conducted manually, introducing a potential difference between the chosen arrival time and the actual arrival time. The picking error used in this inversion process is set as 1ms.

Constraints play an important role in the inversion process, ensuring that the resulting model remains to certain physical expectations. In this context, three key constraints are applied: disturbance, minimum velocity, and maximum velocity. The disturbance constraint regulates the maximum allowed change in average velocity per iteration, preventing rapid changes and contributing to the smoothing of the inversion process. The minimum velocity constraint establishes a lower limit for velocity values, prevent any unrealistic solutions with very low or negative velocities. Conversely, the maximum velocity constraint imposes an upper limit on velocity values to prevent the generation of unrealistic solutions with excessively high velocities. In this inversion process, the constraint distribution is set at 70%, with a minimum velocity of 400 m/s and a maximum velocity of 2000 m/s. These values are deemed acceptable as the initial model encompasses a velocity range from 500 m/s

to 1700 m/s. A minimum velocity constraint of 400 m/s ensures that the inversion process captures the lowest geological features, while a maximum velocity constraint of 2000 m/s ensures the capture of the wall with a velocity of 1700 m/s. The constraint distribution is set at 70% to ensure that the maximum change in average velocity per iteration is suitable for examining the wall structure with its real velocity.

Smoothing is a critical parameter in seismic inversion, serving as a regularization technique to strike a balance between fitting the observed data and obtaining a model that is both accurate and geologically reasonable. This involves considerations such as horizontal smoothing length, vertical smoothing length, smoothing weighting factor, and smoothing scalar.

Horizontal smoothing length dictates the lateral distance over which the inversion process takes neighbouring cells into account for smoothing the model. The default setting for horizontal smoothing is 10 times the horizontal spacing set in the modelling parameters. However, the horizontal smoothing is slightly decreased to better capture the limited lateral variation in the initial model. This adjustment is made to prevent the smoothing process from cloaking the wall structure.

Similarly, the vertical smoothing length determines the vertical distance over which adjacent layers are considered for smoothing the model. The default setting for vertical smoothing is 5 times the vertical spacing set in the modelling parameters. However, we slightly increased the vertical smoothing to enhance clarity in visualizing the wall structure in depth.

The smoothing weighting factor determines the influence of the smoothing term relative to the data-fitting term in the inversion. It is expressed as a percentage, indicating the weight assigned to the smoothing term. The default setting for the weighting factor is 80%, but using this value resulted in an overly smooth inverted model, hiding the wall structure. Consequently, the weighting factor was reduced to 40%.

The smoothing scalar represents the intensity of smoothing at each iteration of the inversion. A larger smoothing scalar per iteration intensifies the impact of smoothing, making the model smoother with each iteration. The default setting for the smoothing scalar is 0.95, but this resulted in excessive smoothing, simplifying the model too much. Consequently, the smoothing scalar was adjusted to 0.8 for a more balanced inversion.

In summary, each parameter for the model is carefully set to ensure the retrieval of a reliable and accurate inverted model. Figures 26 and 27 shows the final inverted model for this synthetic model .

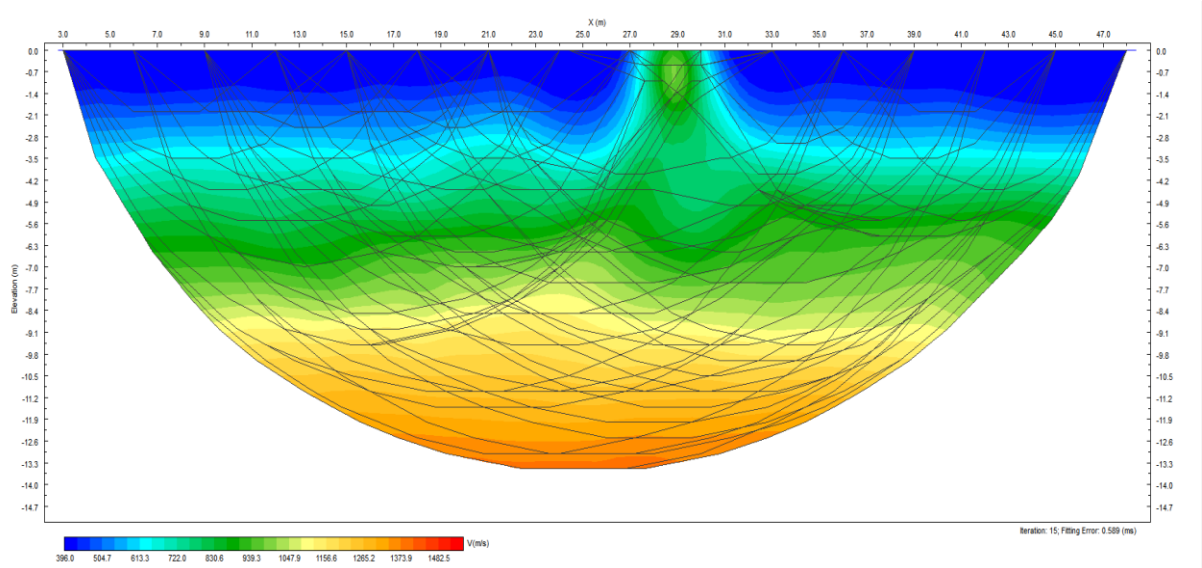

Figure 26: Final inverted model for 2D synthetic model with ray-path

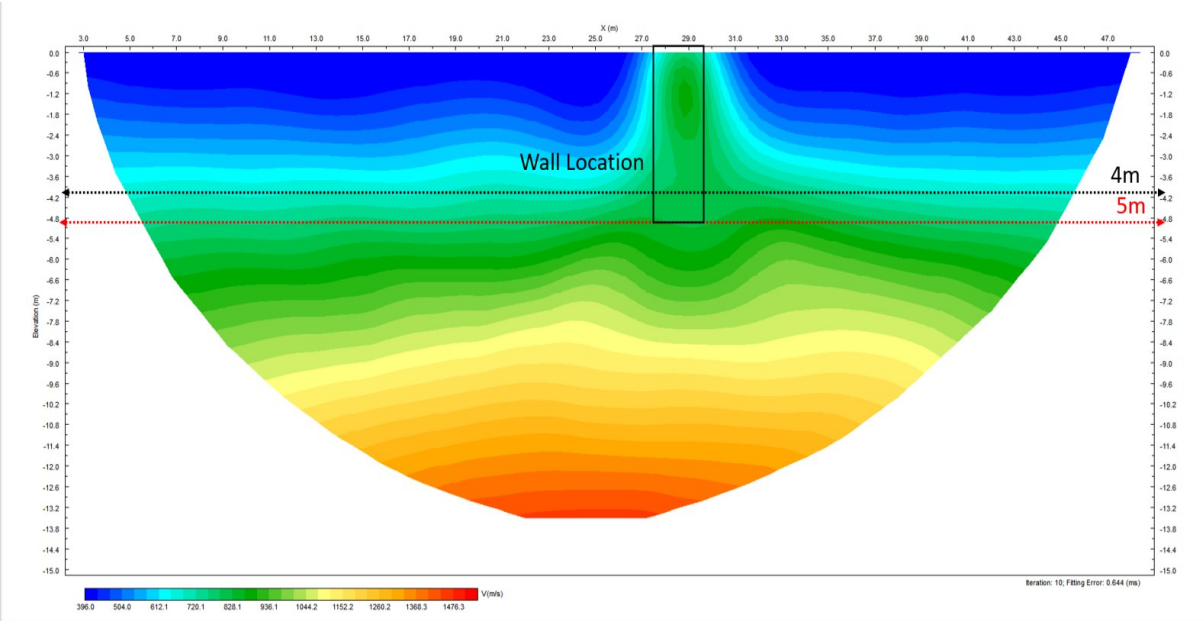

Figure 27: Final inverted model for 2D synthetic model

The inverted model provides valuable insights. The lateral location of the wall is accurately identified between 27.5m to 29.5m. However, the depth of the wall is not clearly identifiable in the inverted model. In the initial model, the wall is positioned at 5m depth, and while the inverted model does exhibit velocity variation up to 5m vertically, the exact depth of the wall is not distinctly visible. Additionally, the velocity values in the inverted model do not precisely represent the true velocity of the wall. In the initial model, the wall has a velocity of 1700 m/s, while the inverted model indicates a velocity range between 800-1000 m/s. The velocity variation in the two subsurface layers is discernible, but the velocity of the second layer in the inverted model appears lower than in the initial model.

4.2.3 2D Refraction Tomography for Field Data

In 2D refraction tomography for field data, only the data from the first horizontal line, as shown in Figure 28, is used to generate the refraction tomography. Specifically, shots 1, 3, 6, 8, 10, 12, 14, and 16, totalling 8 shots, are taken into consideration.

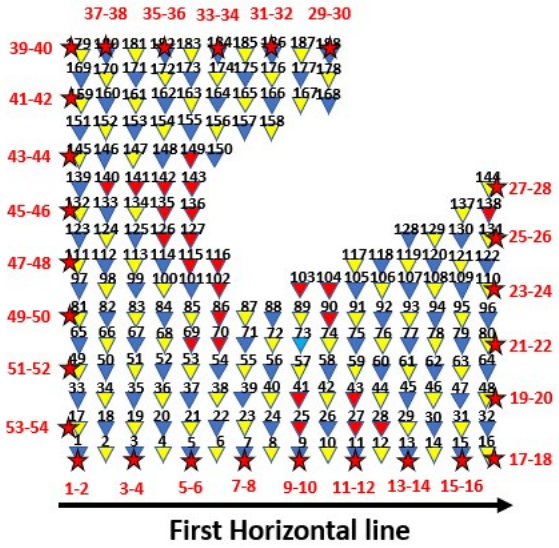

Figure 28: The shots and receivers position used for field data

The distance interval between the receivers remains consistent with the distance used in the synthetic model, which is 3m. The same gradient model is used to create the initial model, with depths ranging from 0 to 15m and velocities varying between 500 and 1700 m/s. The parameters established for the synthetic model inversion are applied to the field data as they have proven to be effective and sufficient for visualizing the subsurface structure as shown in below.

For Modelling:

Spacing (m): Horizontal = 0.4, Vertical = 0.5

Order: Horizontal = 6, Vertical = 6

For Inversion

Maximum iteration = 10

Picking Error (ms) = 1

Distribution (%) = 70

Minimum velocity (m/s) = 400

Maximum velocity (m/s) = 2000

Horizontal smoothing (m) = 3

Vertical smoothing (m) = 3

Weighing (%) = 40

Scalar smoothing = 0.8

With these parameters, the inverted model has been generated, revealing the subsurface structure, including the wall, as illustrated in Figure 29.

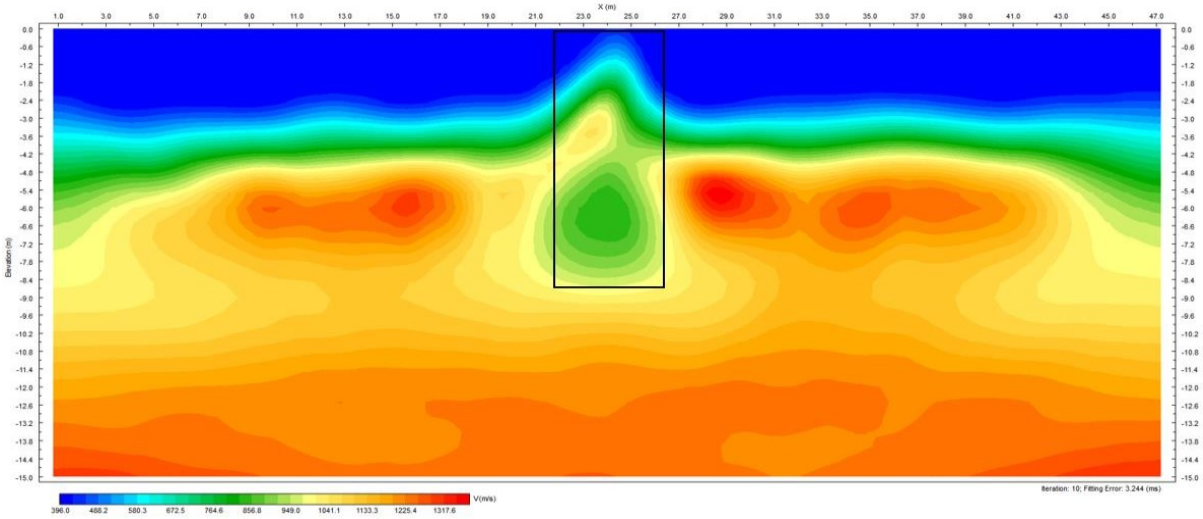

Figure 29: Inverted model for field data with the presence of wall

4.2.4 Pseudo-3D Synthetic Initial Model and 3D Refraction Tomography

In Figure 30**,** the 3D initial synthetic model is presented. Instead of creating a true 3D synthetic model, a pseudo-3D synthetic initial model has been generated using the 2D initial model Geogiga software. This pseudo-3D model includes five vertical and five horizontal survey lines. It consists of two subsurface layers and two walls, each having different physical properties. The first wall extends 8m in the x-direction, 2m in the y-direction, and 8m in depth from the surface. Meanwhile, the second wall measures 2m in the x-direction, 8m in the y-direction, and 6m in the z-direction, as illustrated in Figure 31. The velocities for the first layer and second layer are 500 m/s and 1500 m/s, respectively. Both walls have a velocity of 1700 m/s. As mentioned earlier, there are a total of 10 survey lines—5 in the vertical direction and 5 in the horizontal direction. Each line is equipped with 11 geophones spaced 2m apart. The dimensions of this pseudo-3D model are 20 x 20 x 20m.

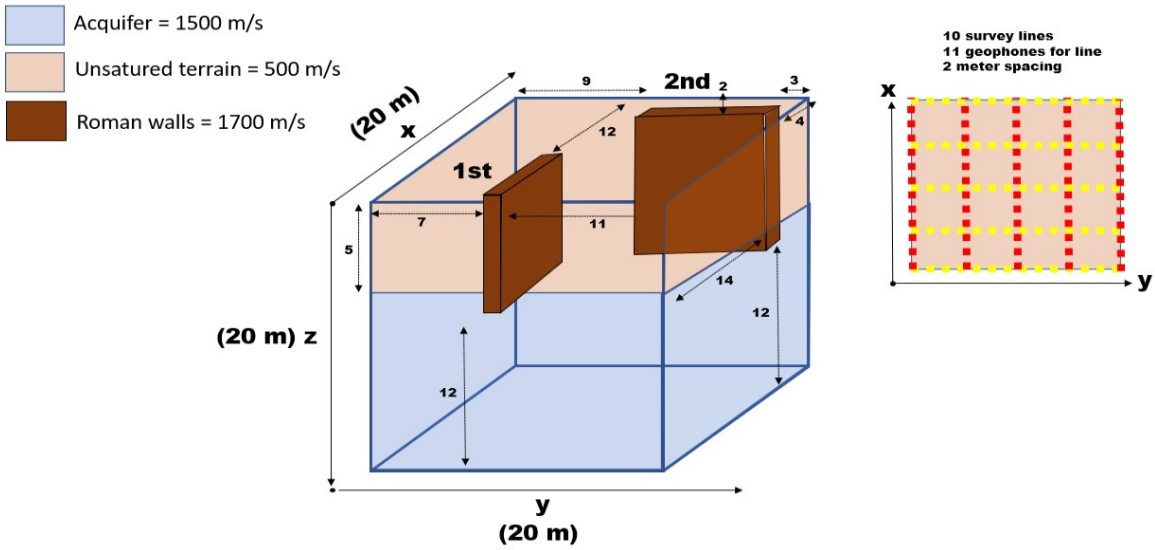

Figure 30: 3D Synthetic initial model

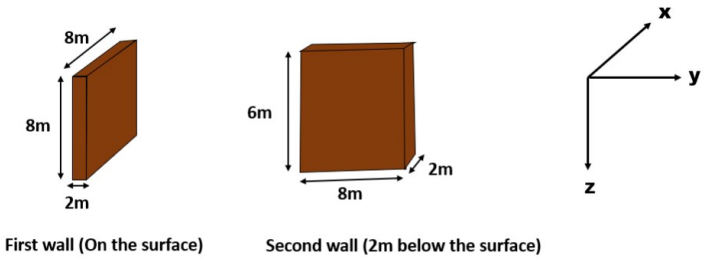

Figure 31: Dimensions of the walls

Five 2D initial models have been generated to produce the pseudo-3D synthetic data, as shown in Figure 32. The survey lines in the x-direction exclusively intersect the second wall, specifically lines 3 and 4. On the other hand, the survey lines in the y-direction intersect both walls—lines 1 and 2 cross the first wall, while line 4 crosses the second wall.

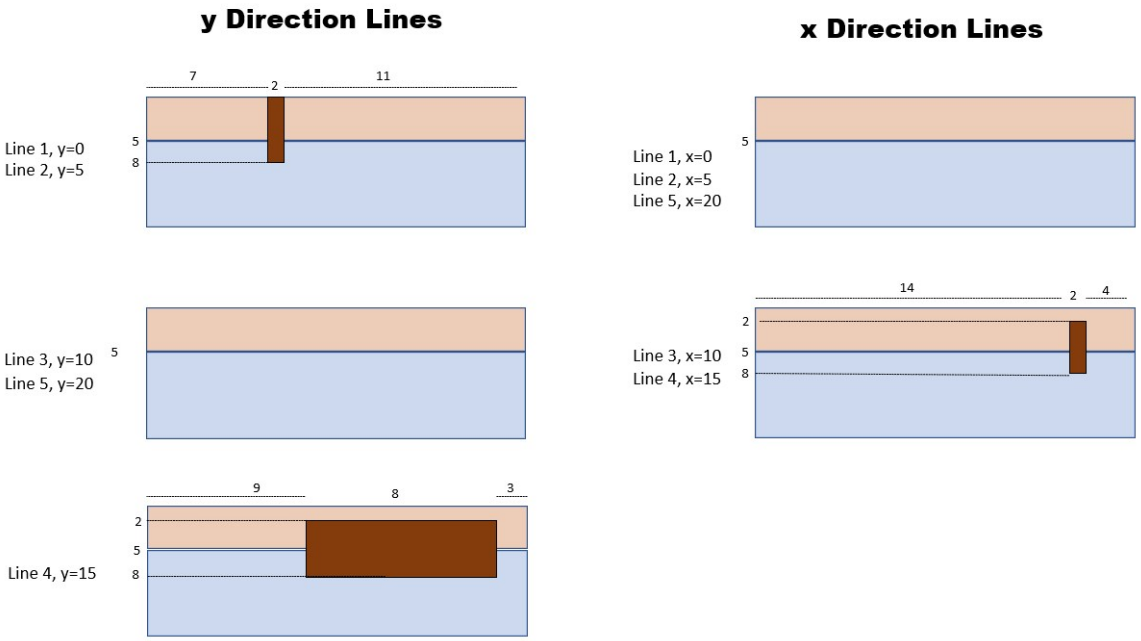

Figure 32: Five initial 2D model for Pseudo-3D Synthetic initial model

For survey lines 1, 2, and 5 in the x-direction, located at distances x=0, x=5, and x=20, respectively, and survey lines 3 and 5 in the y-direction, located at distances y=10 and y=20 respectively, the initial model is straightforward, consisting of only two subsurface layers without the presence of a wall, as shown in Figure 33. The source positions in these initial models are 0, 4, 8, 12, 16, 20, and 22m, totalling 7 shots, while the receiver positions are 1, 3, 5, 7, 9, 11, 13, 15, 17, 19, and 21m, totalling 11 receivers.

Figure 33: 2D Synthetic initial model for survey lines 1,2 and 5 (x-direction) and survey lines 3 and 5 (y-direction)

For survey lines 3 and 4 in the x-direction, located at distances x=10 and x=15, respectively, the initial model incorporates a 2m-wide subsurface wall (2nd wall), positioned 2m beneath the surface, with a

height of 6m as illustrated in Figure 34. The positions of both sources and receivers remained consistent with the previously used configuration.

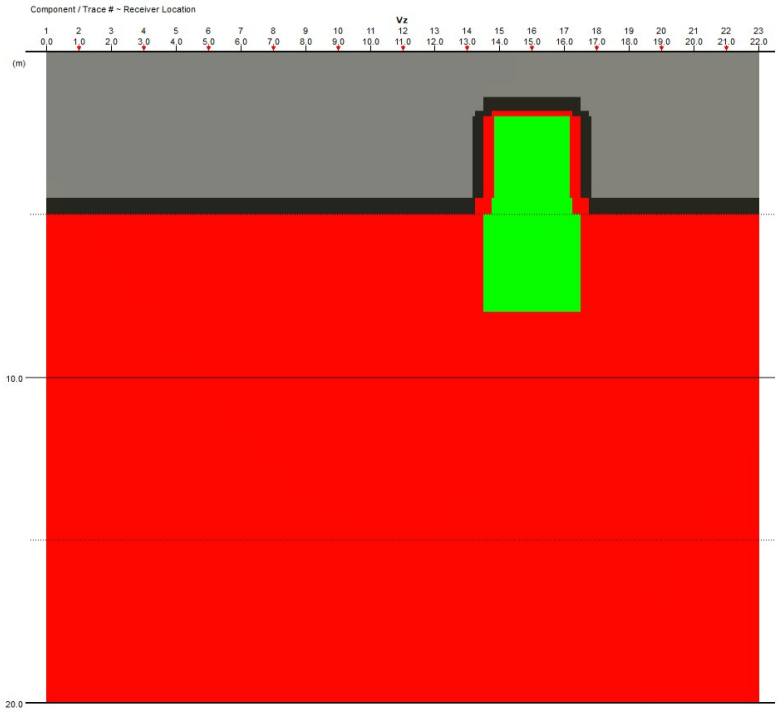

Figure 34: 2D Synthetic initial model for survey lines 3 and 4 in x-direction

Meanwhile, for survey lines 1 and 2 in the y-direction, located at distances y=0 and y=5 respectively, the initial model includes the first wall at the surface with dimensions of 2m in the x-direction and 8m in depth, as illustrated in Figure 35. The source positions in these initial models are 0, 4, 10, 14, 18, and 22m, totalling 6 shots, while the receiver positions are 1, 3, 5, 7, 9, 11, 13, 15, 17, 19, and 21m, totalling 11 receivers. Utilizing varied source positions serves the purpose of mitigating direct interactions with the wall structure.

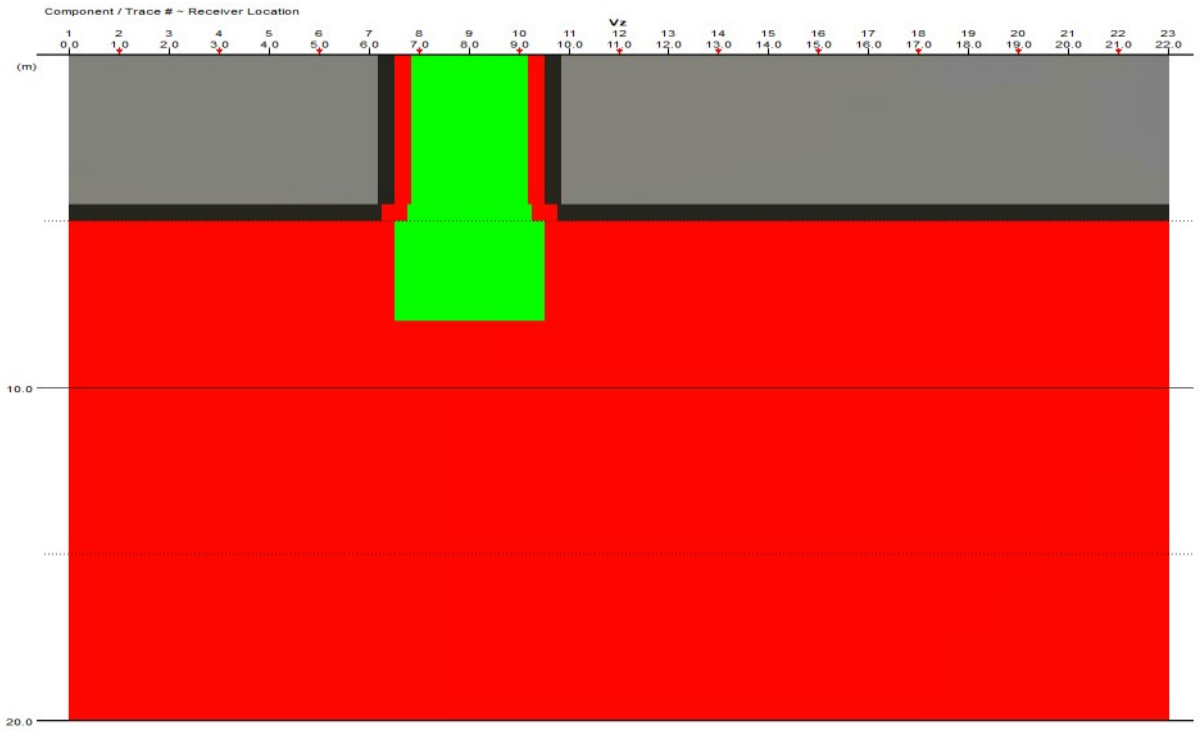

Figure 35: 2D Synthetic initial model for survey lines 1 and 2 in y-direction

Last but not least, for survey lines 4, positioned at distance y=15, the initial model includes the second wall with dimensions of 8m in the x-direction and 6m in depth, as illustrated in Figure 36. The positions of both sources and receivers remained consistent with the previously used configuration in x-direction.

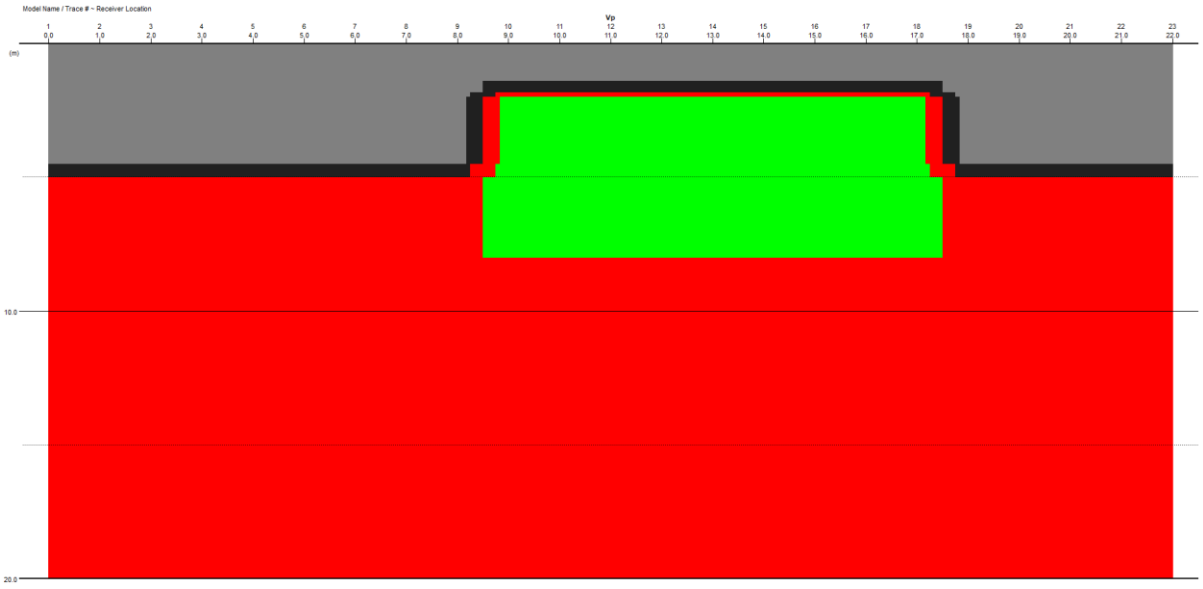

Figure 36: 2D Synthetic initial model for survey line 4 in y-direction

After setting up for the pseudo-2D initial model, the same procedure in 2D tomography is executed to obtain the first break picking. Similar to the 2D tomography, 3D tomography also require to set an initial model to initialize the 3D inversion process. The maximum inverted depth is set as 10m with the distance of 0-22m for both x and y direction with the interval of 1m. The model is set with the range from 0-10m and velocity varying from 200 to 2000 m/s.

The parameters used for this 3D synthetic model inversion are shown in below:

For Modelling:

Spacing (m): x=1, y =1 and z =1

Order: x= 5, y= 5 and z= 5

For Inversion:

Maximum iteration = 20

Picking Error (ms) = 0.2

Distribution (%) = 40

Minimum velocity (m/s) = 200

Maximum velocity (m/s) = 2500

x-direction smoothing (m) = 7

y-direction smoothing (m) = 7

z-direction smoothing (m) = 5.5

Weighing (%) = 60

Scalar smoothing = 0.8

In the 3D inverted synthetic model, a maximum of 20 iterations is used to achieve a more complex model while providing a clearer representation of the wall's location. The smoothing values for the x and y directions are decreased, and the smoothing in the depth (z-direction) is slightly increased from the default setting of 5m, aligning with the principles established in the 2D initial model. Figure 37 shows the two walls location on the surface.

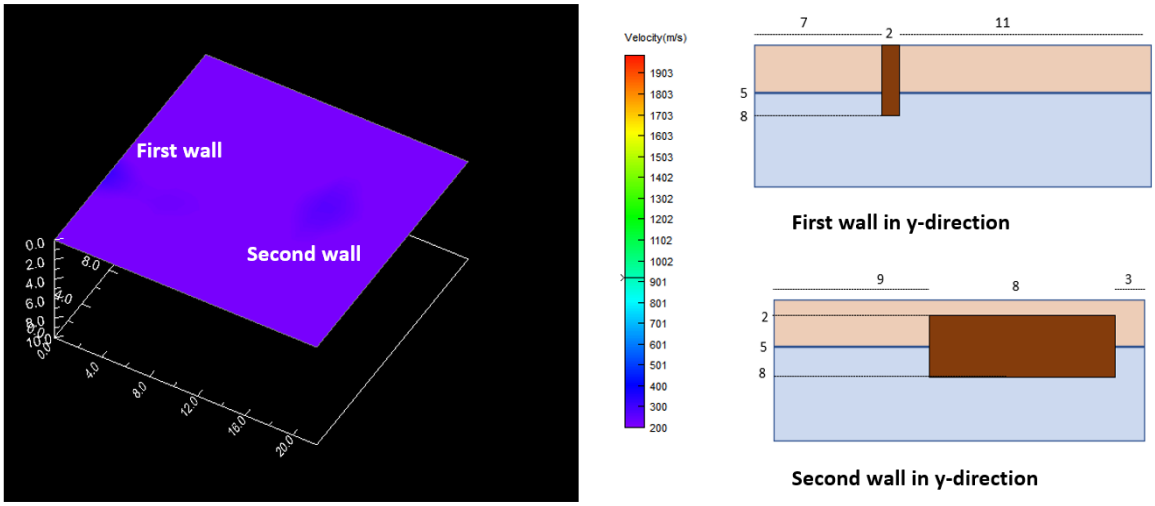

Figure 37: Two walls location on the surface and the walls location in y-direction

At a depth of 2m, the visibility of the walls becomes more pronounced, characterized by velocities ranging from 1000 to 1400 m/s. It is noteworthy that the onset of the second wall is specifically

identified at the depth of 2m, highlighting the success of the inverted 3D model in capturing the appearance of the second wall at this depth as illustrated in Figure 38.

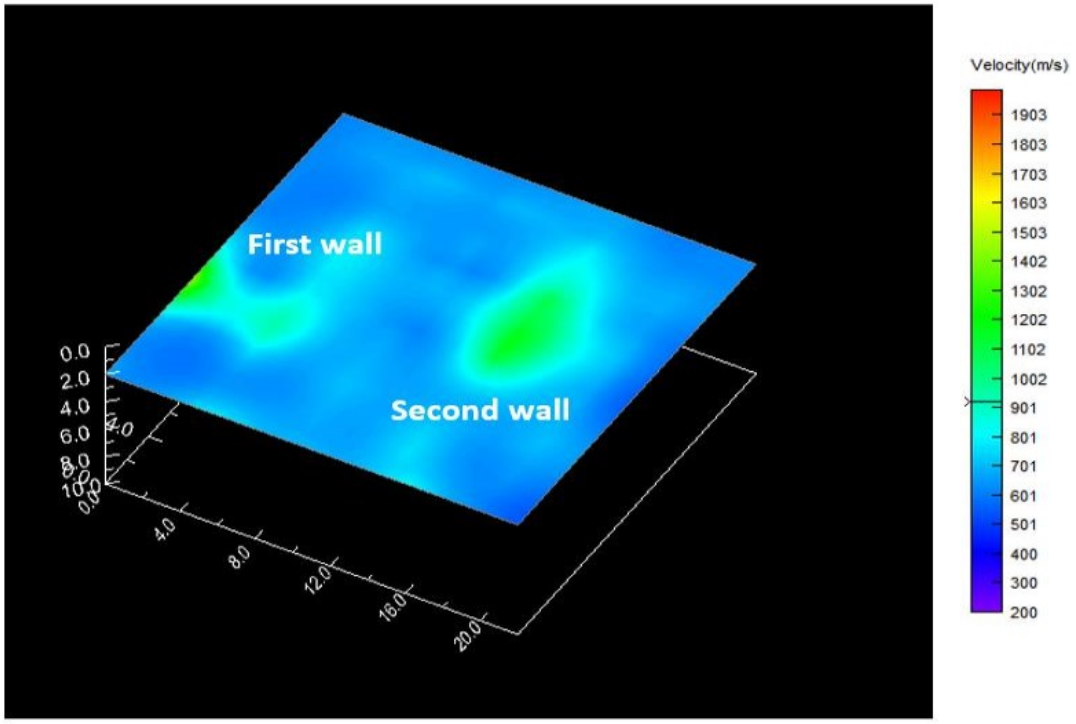

Figure 38: Walls location in 2m depth

The appearance of the two walls go on at depths of 4m and 6m, exhibiting velocities within the range of 1600 to 1900 m/s as illustrated in Figure 39. It is noteworthy that these velocity values align with the predefined velocity of the walls set in the 3D synthetic initial model.

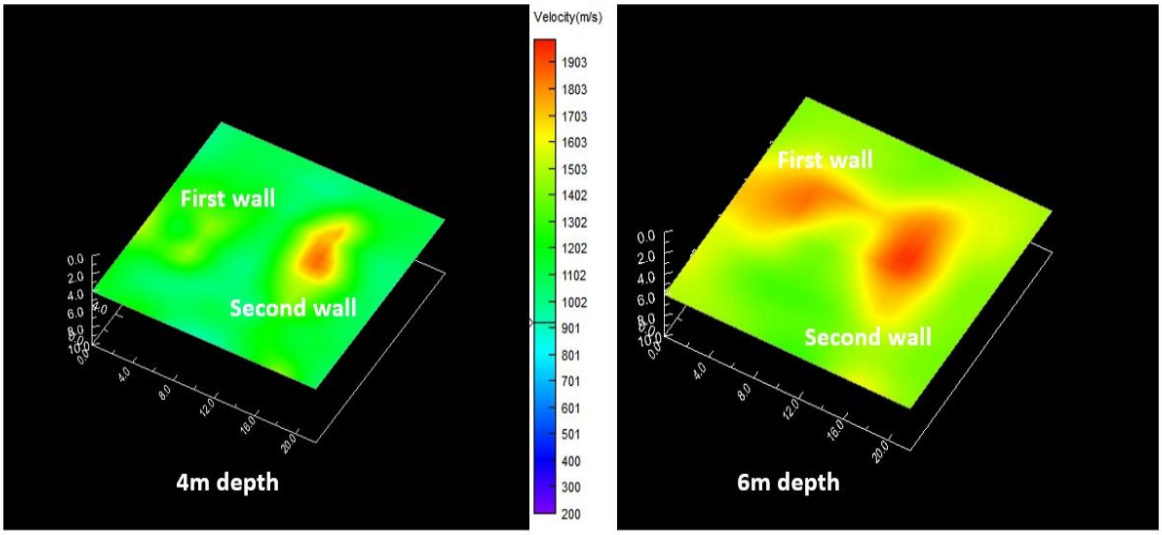

Figure 39: Walls location in 4m and 6m depth

Both walls end at a depth of 8m, and the second layer (aquifer) is characterized by a velocity of 1500 m/s. The inverted model shows a homogenous velocity at 8m depth ranging from 1700 to 1800 m/s,

which appears slightly higher compared to the actual velocity specified in the 3D synthetic initial model, as illustrated in Figure 40.

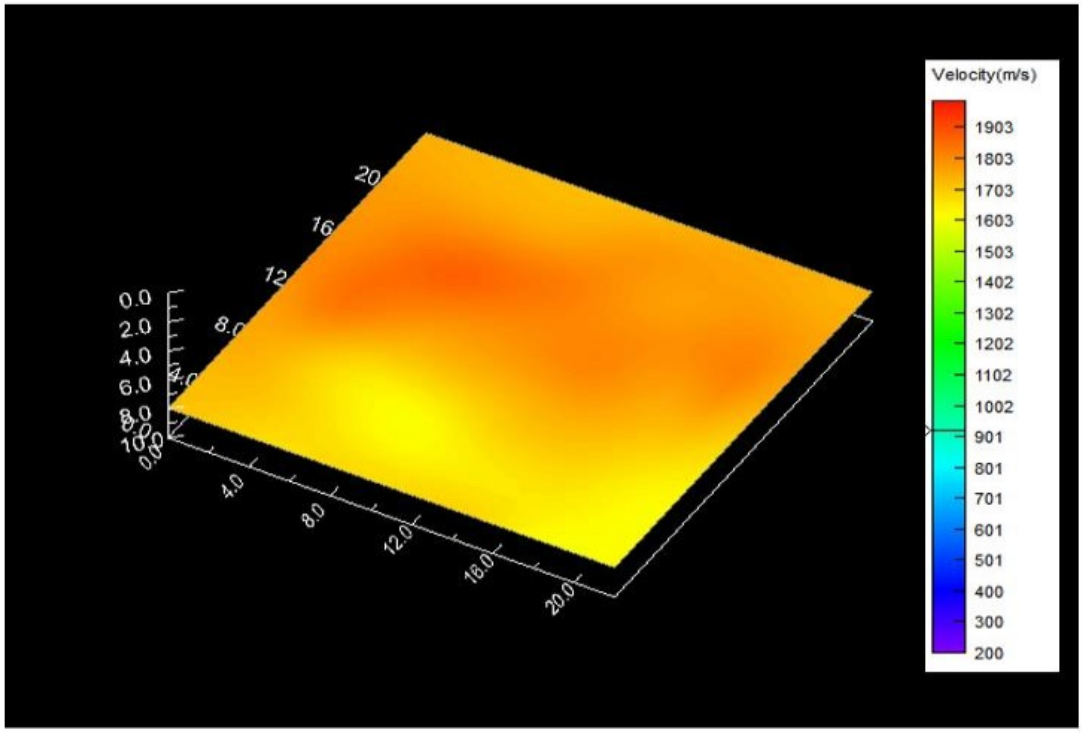

Figure 40: The inverted model of 8m depth

A cross-sectional view in the x-direction is presented in the inverted 3D model, revealing the presence of two walls at x=0 and x=14m, consistent with the specifications in the initial model, as illustrated in Figure 41.

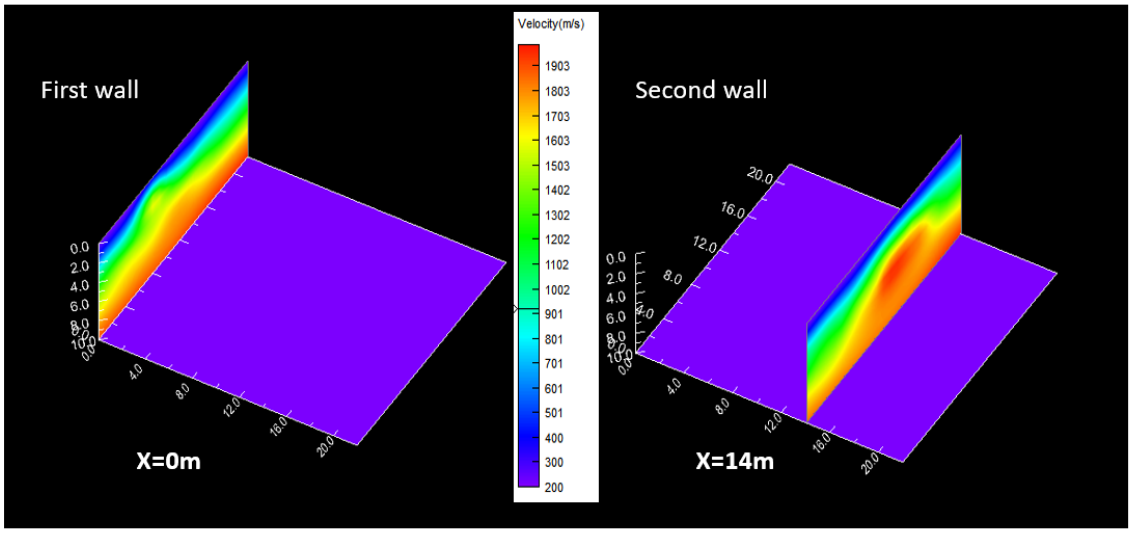

Figure 41: Slide in x-direction at x=0m (left) and x= 14m (right)

4.2.5 3D Refraction Tomography for field data

In 3D refraction tomography for field data, the first break picking data is used for shots in the South-North direction, considering all available receivers. It is worth noting that some receivers may lack picking data due to excessive noise hence they were unsuitable for the picking process.

In the initial model for 3D refraction tomography, the maximum inverted depth is set at 10m, with the velocity ranging from 500 to 2000 m/s. The specific parameters used for the inversion of this 3D model are outlined below:

For Modelling:

Spacing (m): x= 1.5, y =1.5 and z =0.8

Order: x= 6, y= 6 and z= 6

For Inversion

Maximum iteration = 10

Picking Error (ms) = 0.6

Distribution (%) = 70

Minimum velocity (m/s) = 400

Maximum velocity (m/s) = 2000

x-direction smoothing (m) = 13

y-direction smoothing (m) = 13

z-direction smoothing (m) = 3

Weighing (%) = 40

Scalar smoothing = 0.8

It is noteworthy that several parameters have been adjusted in this inverted model compared to the 3D inverted synthetic model. The order is slightly increased due to the complexity of the survey area. The picking error is increased as the obtained data exhibit noise, making it more challenging to obtain accurate first break picking compared to the synthetic model. Furthermore, the maximum number of iterations is decreased to 10, as 20 iterations produced a too complex inverted 3D model in this inversion. Regarding smoothing, it is slightly decreased in all directions compared to the default setting to avoid over-smoothing. The outcomes of the 3D refraction tomography will be presented in the subsequent chapter under 'Results.'

4.3 Seismic surface wave tomography

This seismic surface wave analysis is conducted using MATLAB software, and the code is adapted from Barone et al., 2022. The analysis comprises two critical sections: the preliminary analysis and Eikonal Tomography (Phase Velocity Maps) and Auto-Spectrum Gradient Computation.

4.3.1 Preliminary analysis

The primary purpose of conducting the preliminary analysis is to identify the fundamental mode and the presence of higher modes, as well as to find out the frequencies characterizing the surface waves. In surface wave analysis, the phase distribution primarily focuses on a single mode of wave propagation, typically the fundamental mode of Rayleigh waves. This preliminary analysis aims to identify and eliminate any coherent noise that may exhibit consistency and predictability across the signals. Such noise can disrupt both phase and amplitude variations with offset, leading to the generation of periodic patterns (Barone et al., 2022). Coherent noise sources include higher modes of propagation, vibrations from the sources, and backscattering.

To conduct the preliminary analysis of the dataset, it is crucial to first understand the survey area's geometry. In this analysis, only one shot, which is labelled as "shot 1-2," was used as illustrated in Figure 42. The analysis considered two receiver lines: one oriented from South to North and the other from West to East, with a total of 16 receivers installed in each line.

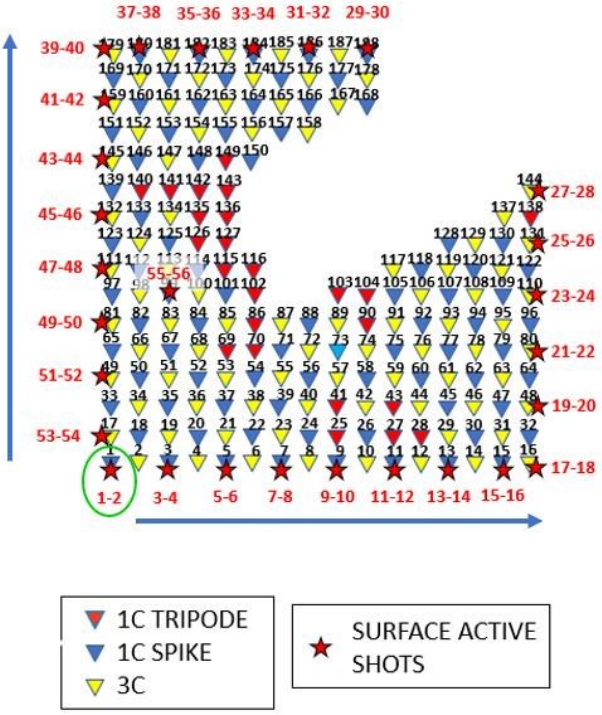

Figure 42: Two receiver lines in South to North and West to East Direction

This processing scheme of the raw 3D data is based on the MATLAB coding provided by Barone et al., 2020. The preliminary analysis comprises both 2D and pseudo-3D analyses. Initially, the 2D analysis is conducted. Seismograms from both the horizontal and vertical receiver lines can be visualized in Figure 43, where time is plotted on the y-axis, and offset is plotted on the x-axis.

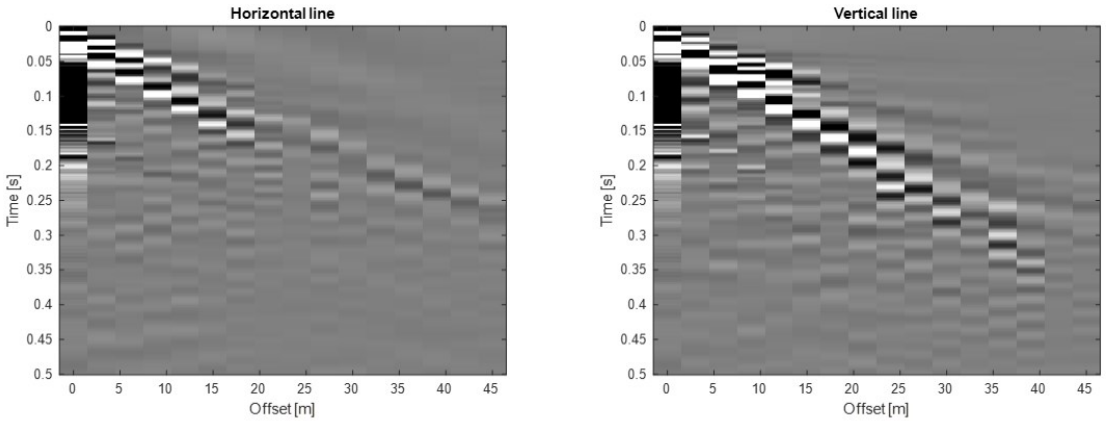

Figure 43: Seismograms for lines in West to East (Left) and South to North (Right) Direction

Following this, a 2D Fast Fourier Transform (FFT) is performed on both traces to compute the *f-k* spectrum. The computation of *f-k* spectrum aims to identify the presence of higher modes and provide a preliminary understanding of the seismic velocities and frequencies of the surface waves. Figure 44 shows *f-k* spectrum and turned *f-k* spectrum for horizontal line in West to East direction.

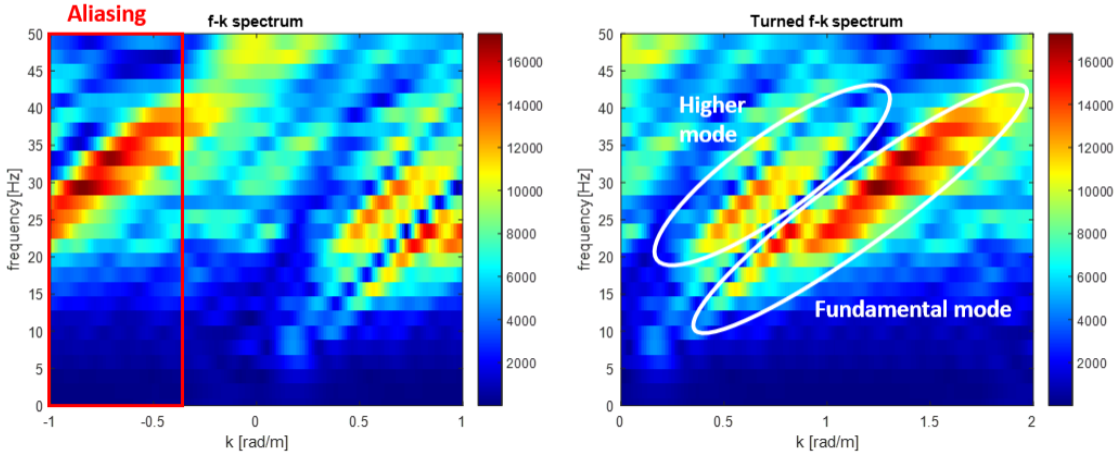

Figure 44: *f-k* spectrum and turned *f-k* spectrum for line in West to East direction

The image on the left side of the figure illustrates the aliasing effect. Spatial aliasing occurs due to the low phase velocities of the surface wave and insufficient spatial sampling. To prevent aliasing, the wavenumber of the signals should be lower than the Nyquist wavenumber for all frequencies. Nyquist-Shannon sampling theorem states that the Nyquist wavenumber is equal to the half of the sampling wavenumber and half of the inverse of the distance between the geophones. In this analysis, the spatial sampling is too big compared to the signal wavenumber leading to their manifestation in the negative wavenumber domain, despite originating from higher positive wavenumbers. A turned f-k spectrum is computed to compensate for the aliasing effect as shown in Figure 42, in which the signal in the negative wavenumber, induced by aliasing, is now properly displayed in the positive wavenumber domain. The frequency band relevant to the fundamental mode spans from 10 to 50 Hz

and will be used for the subsequent analysis. Despite the low resolution, different orders of higher modes are visible.

After the 2D analysis, a pseudo-3D analysis is performed. This 3D data set is sorted by offset which allows for the observation of how seismic wave characteristics, such as arrival times, change with the distance between the source and receivers, as illustrated in Figure 45.

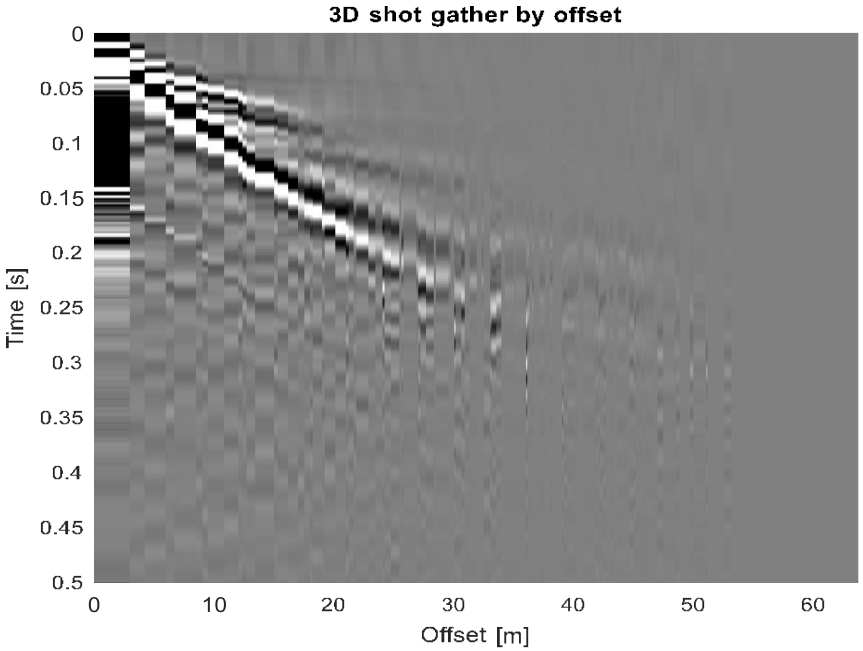

Figure 45: 3D shot gather by offset

The dataset is further regularized to provide regularly spaced offsets for the computation of *f-k* spectrum as illustrated in Figure 46.

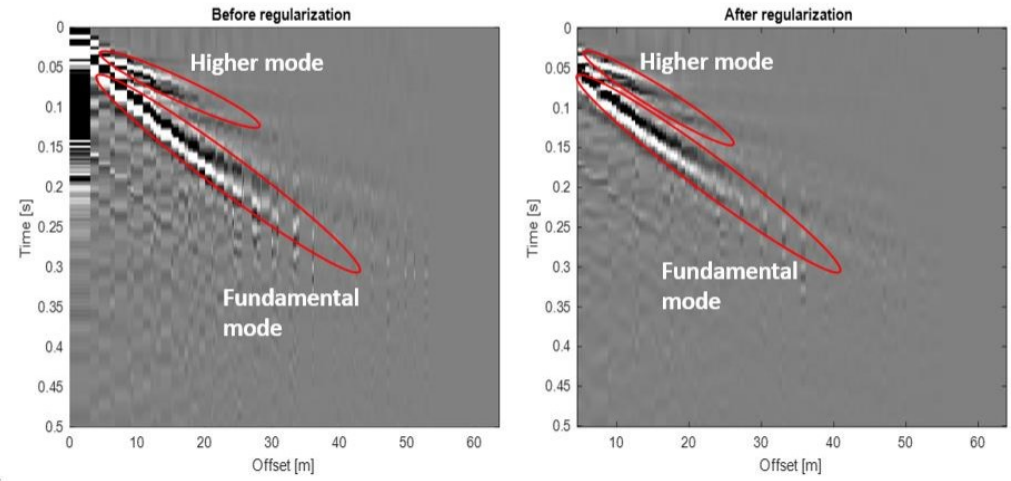

Figure 46: 3D dataset before and after regularisation

Same as 2D analysis, the FFT is performed to compute the f-k spectrum for 3D analysis. After the computation of f-k spectrum, a manual picking was performed to pick the dispersion curve that separates the fundamental mode from higher mode as illustrated in Figure 45**.** The selected dispersion curve will serve as the relationship between Linear Moveout velocities (LMO) and frequency for the subsequent 3D processing. Additionally, Figure 47 demonstrates improved resolution in the f-k spectrum compared to the 2D analysis due to the increased amount of data.

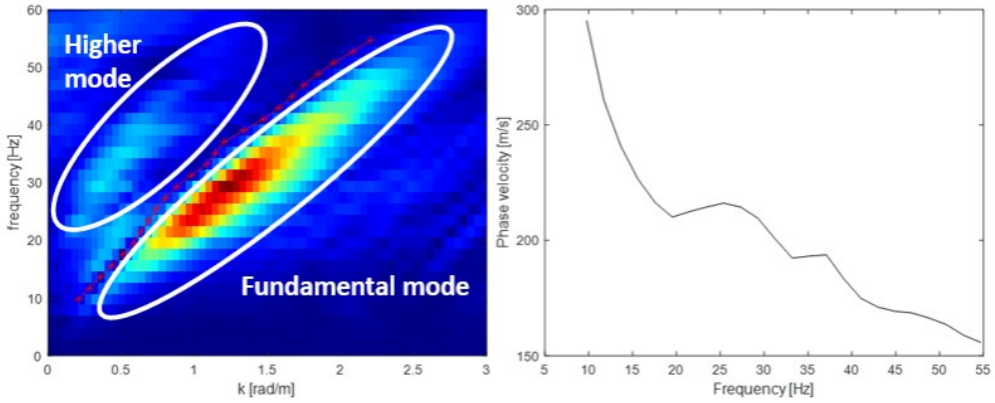

Figure 47: *f-k* spectrum and selected dispersion curve for 3D dataset

4.3.2 Eikonal Tomography (Phase Velocity Maps) and Auto-Spectrum Gradient Computation

Following the retrieval of the interested frequency range and Linear Moveout Velocity (LMO) from the preliminary analysis, the computation of auto-spectrum gradient and generation of phase velocity maps (Eikonal Tomography) are conducted. The information from all the shots and receivers are extracted for the analysis. The best shots are selected for analysis, taking into account that each location consists of a total of two shots. The selected shots for analysis include shot 1, 3, 6, 8, 10, 12, 14, 16, 17, 20, 22, 24, 26, 28, 29, 32, 34, 36, 38, 40, 41, 43, 45, 48, 50, 52, 54 and 56. The frequency range chosen for this analysis is between 10 Hz to 50Hz. This range was chosen based on the preliminary analysis, which indicated that the majority of the surface wave energy is concentrated within this frequency range in the survey. The frequencies were 10 Hz, 10.98 Hz, 12.16 Hz, 13.64 Hz, 15.52 Hz, 18 Hz, 21.43 Hz, 26.47 Hz, 34.62 Hz and 50 Hz.

Before the computation of the auto-spectrum gradient, a limit for near-offset is set. The near-offset in this analysis is set as half of the wavelength of signal and the data with wavelength less than the near offset is excluded from this analysis because the surface wave may not have fully developed yet in the near offset, as it requires some time to fully develop and propagate. Therefore, the seismic signals recorded at near offsets might not provide the complete representation of the surface wave data needed for this analysis.

The computation of auto-spectrum gradient involves examining the rate of amplitude change of the signal respect to its offset. This process quantifies how rapidly the amplitude varies with spatial variation (offset). Auto-spectrum gradient computation is an essential step in this analysis because many tomography methods carried out, such as Eikonal tomography, rely on high-frequency approximations. In these methods, the lateral resolution is constrained by the signal's wavelength, and higher frequencies correspond to shorter wavelengths. This computation helps to improve the tomography approach by understanding how frequency affects amplitude**.** Auto-spectrum gradient computation is an essential method for identifying sudden lateral velocity variations due to subsurface discontinuities and other objects. By examining the variations in amplitudes of surface waves across

different signal frequencies, this approach able to obtain the derivation of velocity variations within the subsurface.

Auto-spectral density quantifies how the energy of a signal's surface wave is distributed across different frequencies. The auto-spectral density for each frequencies G(f) is analysed as described in Equation 12. In this equation, Y represents the complex spectrum, and A corresponds to the amplitude spectrum of a seismic record.

$$G(f)= \{ Im [Y(f)] \}^2 + \{ Re [Y(f)] \}^2 = \{A (f) \}^2 \qquad (12)$$

The auto-spectrum gradient maps can be produced by first retrieving the auto-spectral density maps for all the shots. The obtained values are normalized by dividing each value by the maximum value in order to ensure that the data remains within the range of 0 to 1. Then, the auto-spectrum gradient is computed. This involves calculating the gradient of the auto-spectral density, which includes determining the rate of change of amplitude at each frequency. Through this analysis, we obtain a reliable estimation of the spatial variations in energy, even though it does not show the positive or negative sign of the anomalies but the energy spatial variations can be seen easily.

The 3D processing sequence for the phase velocity maps consist of three main steps. First, a linear moveout (LMO) correction is applied to the raw traces to separate the fundamental mode and higher modes by moving the higher modes energy to the negative wavenumber quadrant of f-k spectrum. Furthermore, LMO correction also help to reduce phase jumps related to the 2π periodicity of the phase. In LMO correction, velocity is a crucial parameter used to calculate the time shifts necessary for aligning data from different offsets. The velocity used for this correction is derived from the preliminary analysis. The amount of time shift applied depends on the offset, as described in Equation 13.

$$\Delta t = \frac{x}{Vlmo} \qquad (13)$$

In the equation, the variable x represents the offset, and Vlmo stands for the velocity used for correction. This correction process flattens linear events with a velocity of Vlmo, while events with higher velocities exhibit a negative moveout. Vlmo serves as a reference velocity, which is obtained from previous analyses. Linear events with velocities close to Vlmo are flattened by applying minimal time shifts to their arrival times. On the other hand, for events characterized by higher velocities (velocities greater than Vlmo), time shifts are applied in the opposite direction, causing them to exhibit negative moveout. After the correction, the fundamental mode appears on the positive side of the wavenumber quadrant of the f-k spectrum, while higher modes are observed on the negative side quadrant of the spectrum, as illustrated in Figure 48.

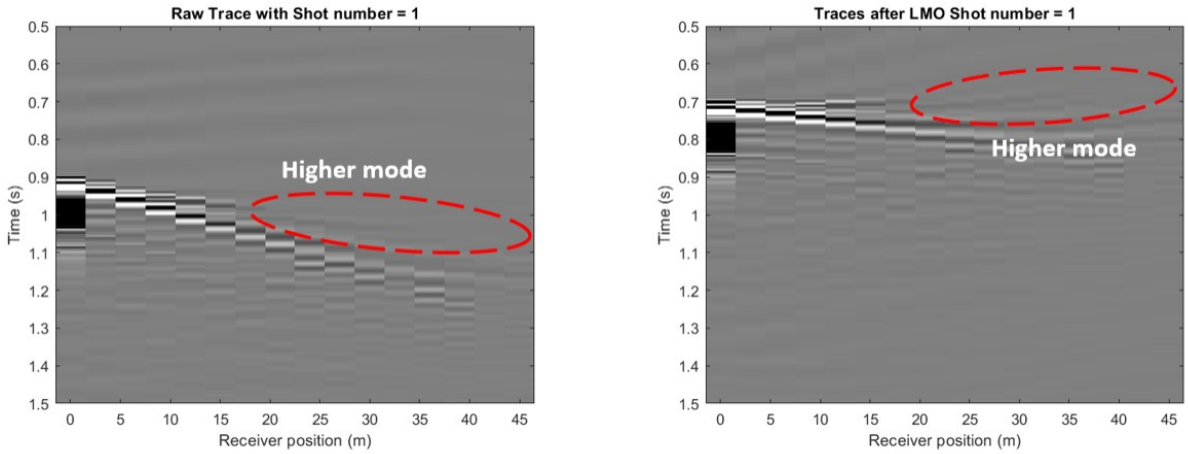

Figure 48: Raw trace and trace after LMO correction

Secondly, pseudo-2D *f-k* filtering over azimuthal sectors is performed. Pseudo 2D *f-k* filter is a filtering applied to the seismic data in the frequency-wavenumber domain and it is often used in the analysis to improve the quality of the signal and noise removal. The term "pseudo 2D" suggests that even though the data is collected in a 3D survey, the processing simplifies the data to focus on two main dimensions. Based on the 3D nature of the acquisition and the regularity of the receiver geometry, a pseudo-2D *f-k* filter is applied on an azimuthal sectors of 5 degrees from the source position, as illustrated in Figure 49.

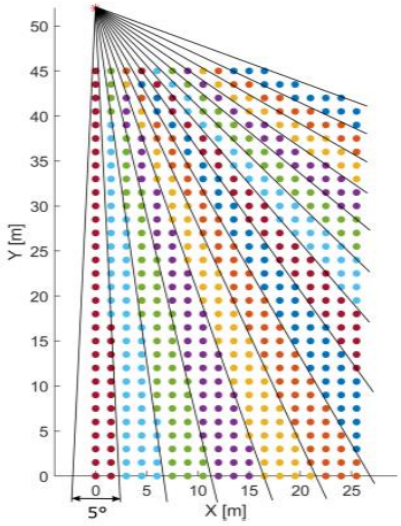

Figure 49: Azimuthal sectors of 5 degrees from source position

For each sectors, spatial separation between the seismic source and the receiver is determined. Then, the seismic traces are interpolated. Following interpolation, the *f-k* spectrum is computed. The filters are arranged to set the spectral amplitude to zero in the positive frequency and negative wavenumber quadrant, while preserving the signal in the positive wavenumber quadrant.

The filtered signals is then retrieved through a Double Inverse Fourier Transform. This procedure involves consecutively applying two Inverse Fourier Transforms (IFFT). The first IFFT converts the filtered signals from the frequency domain to the time domain. Following that, a second IFFT is conducted to ensure the accurate transformation of the signals back to the time domain, while also ensuring that no artifacts or irregularities occur during this transformation process. Finally, linear interpolation is applied once more to ensure that the signals are restored to their original positions. Azimuthal sectors with fewer than 5 traces are excluded from this analysis, along with both the near offset and far offset regions.

Figure 50 illustrates the effect before and after applying the Pseudo 2D filter in the frequency and wavenumber domain. This analysis refers to a specific frequency of 10 Hz and velocity used for correction of 216.1 m/s.

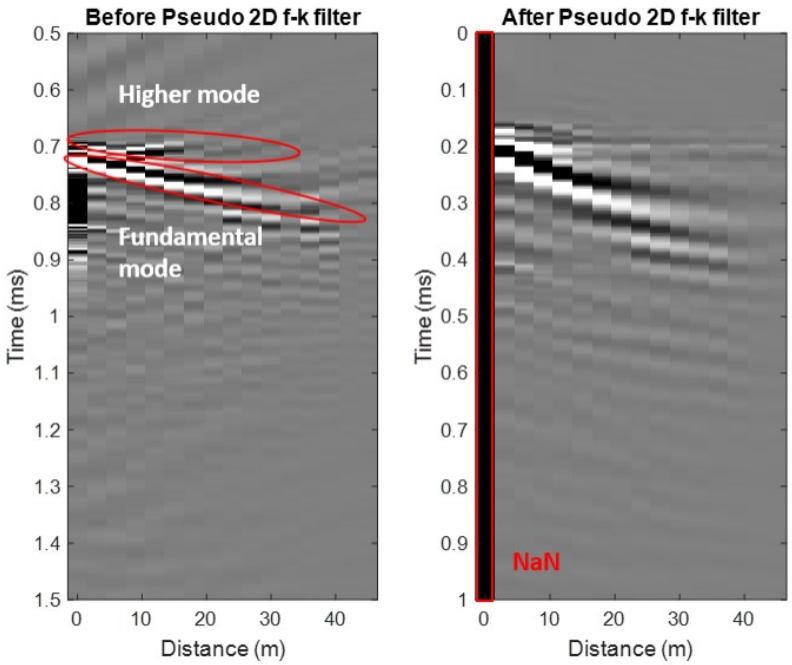

Figure 50: Trace before Pseudo-2D *f-k* filter and trace after Pseudo-2D filter

The Linear Moveout (LMO) correction effectively mitigates most of the phase jumps associated with the 2π periodicity of phase by aligning the arrival times of surface waves at various offsets with a common reference point. However, it is important to note that LMO correction does have its limitations. The choice of Vlmo can potentially lead to overestimation of velocities, given that surface waves can exhibit a variety of velocities depending on the mode of propagation. If the LMO correction velocities are overestimated, it will lead to an overestimation of the expected arrival times at different offsets. Consequently, applying LMO correction with overestimated velocities may result in the arrival times of the fundamental mode at different offsets not aligning perfectly, causing an undercorrection (Barone et al., 2022).

2D phase unwrapping is a processing technique that aims in recovering the original, unwrapped phase values typically ranging from π to -π. When phase values are wrapped, it suggests that phase changes larger than either positive or negative π are not accurately displayed, leading to the appearance of data discontinuities. These values are identified and a compensation procedure is applied in four directions: X, -X, Y, and -Y. This correction can be achieved by either adding or subtracting 2π from the phase, and the data point is marked as successfully unwrapped. The unwrapping process ends when all necessary data points have been successfully unwrapped. Subsequently, the LMO corrections are reversed. Removing the LMO correction post-unwrapping ensures that the unwrapped phase is expressed in the original units, enabling more accurate interpretation. Finally, the obtained phase maps can be transformed into relative travel-time maps using Equation 14**.**

$$\Delta t = \frac{\phi - \phi_0}{2\pi f} \qquad (14)$$

Δt in the equation represents the relative travel-time, ϕ is the phase obtained at receivers and ϕ_0 is the phase recorded at the receiver closet to the source and f is the frequency.

The travel-time maps for a specific frequency from all shots are input into an Eikonal Tomography scheme to extract phase velocity maps. The phase slowness at the given frequency can be derived

from the magnitude of the travel-time gradient using Eikonal tomography. Phase slowness is the inverse of velocity and the relationship between phase slowness and velocity is shown in Equation 15.

$$Slowness = \frac{1}{V} \qquad (15)$$

This process is iteratively performed for each shot point, and the resulting phase velocities are ultimately computed as the inverse of the average phase slowness across various shots. This tomography method does not require a conventional inversion process, ensuring a faster and efficient procedure. This is because the gradient of the phase travel-time yields the local phase speed as a function of the direction of wave propagation. This prevents the need for an inversion process to obtain tomography since the gradient essentially functions as the inverse operator, mapping travel time into model values (phase slowness) without the necessity of constructing a forward model first (Lin et al., 2009). Moreover, the regular geometry of our dataset is well-suited for this method, as it avoids the need for 2D travel-time interpolation over a regular grid. This is due to the unreliability of travel-time interpolation schemes near the station area, where both random and coherent noise tend to increase (Lin et al., 2009). Additionally, Eikonal tomography is well-suited for this analysis as it solely relies on relative travel-time information (travel-time differences between two adjacent receivers) rather than absolute travel-time values. Last but not least, uncertainties (errors) in local phase speeds can be estimated with Eikonal tomography by extracting the standard deviation of the phase velocity. In contrast, Eikonal tomography is very sensitive to outliers. Sensitivity arises during the computation of the gradient of the travel-time, as outliers in the data can introduce larger gradients that may dominate the original gradient value. Therefore, a statistical analysis is performed to identify and remove the possible outliers from the phase velocity maps. In this context, outliers are identified as velocity values beyond three times (either more or less) the standard deviation from the spatial mean.

Lastly, the depth of penetration for all frequencies is calculated using Equation 16. As each frequency exhibits different penetration depths, higher frequencies penetrate more shallowly. It is important to note that the maximum depth of penetration is determined using a rule of thumb, where Zmax is calculated as the wavelength divided by 2.5. This analysis does not involve inversion, so the depth of penetration may not accurately represent the true depth.

$$Zmax = \frac{\lambda}{2.5} = \frac{\tilde{v}}{f} \qquad (16)$$

In the equation, Zmax represents the maximum depth of penetration, λ is the wavelength, $\tilde{v}$ is the average velocity for all the shots at specific frequencies, and f is the frequency.

5. Results

This section presents the outcomes of both seismic refraction and surface wave analyses. The seismic refraction results cover the 2D inversion outcomes for both synthetic and real data, as well as the 3D inversion results for real data. On the other hand, the surface wave analysis results cover the auto-spectral findings and phase velocity maps for all frequencies.

5.1 2D Refraction Tomography

Figure 51 displays the ray-path diagram, highlighting that the ray-path penetration extends only up to a depth of 6m. As a result, any information beyond this depth is considered invalid, as there are no ray-paths passing through depths below 6m. Therefore, details below this threshold are disregarded in the analysis. Furthermore, while the aquifer layer beneath the survey area lacks clear definition, the ray-path inverted model provides a preliminary indication of the aquifer's approximate location, with the majority of refraction events occurring in the depth range of 5m to 6m. As shown in Figure 52, the potential location of the Roman wall aligns closely with the interval of 23.5 to 25.5m in the x-direction, exhibiting a width of approximately two meters. This observation is in accordance with the presence of the Roman wall identified in the survey area, as visualized in Figure 53. As previously mentioned, the inverted model lacks precision in determining the velocity of the wall, primarily due to the constrained spacing of the wall in relation to the survey area. Nevertheless, the aquifer layer within the depth range of 5m to 6m exhibits a suitable velocity range, ranging from 1225 to 1500 m/s.

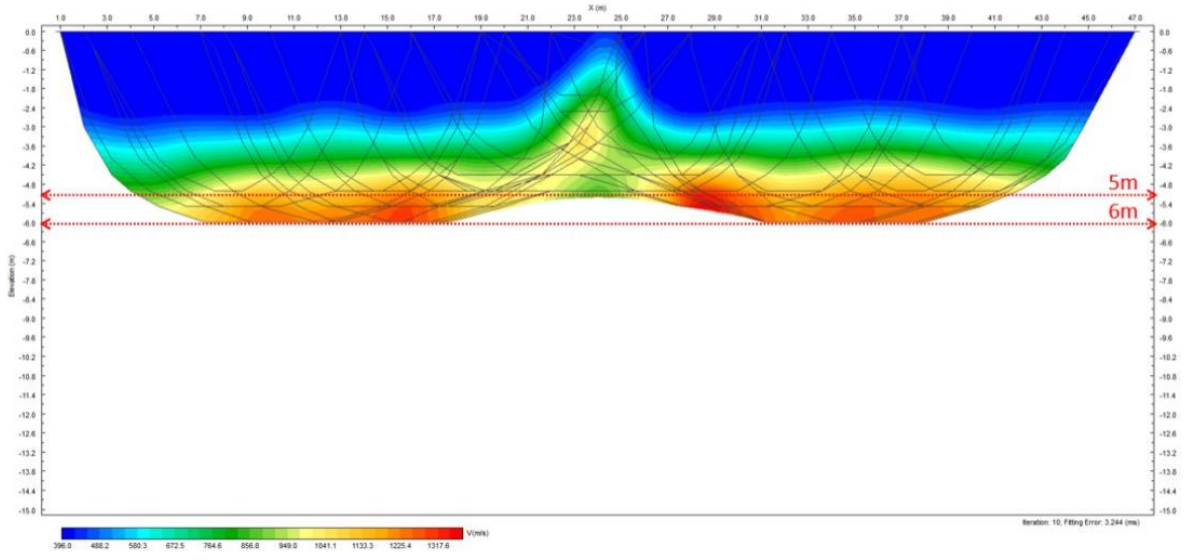

Figure 51: Inverted 2D model with ray-path

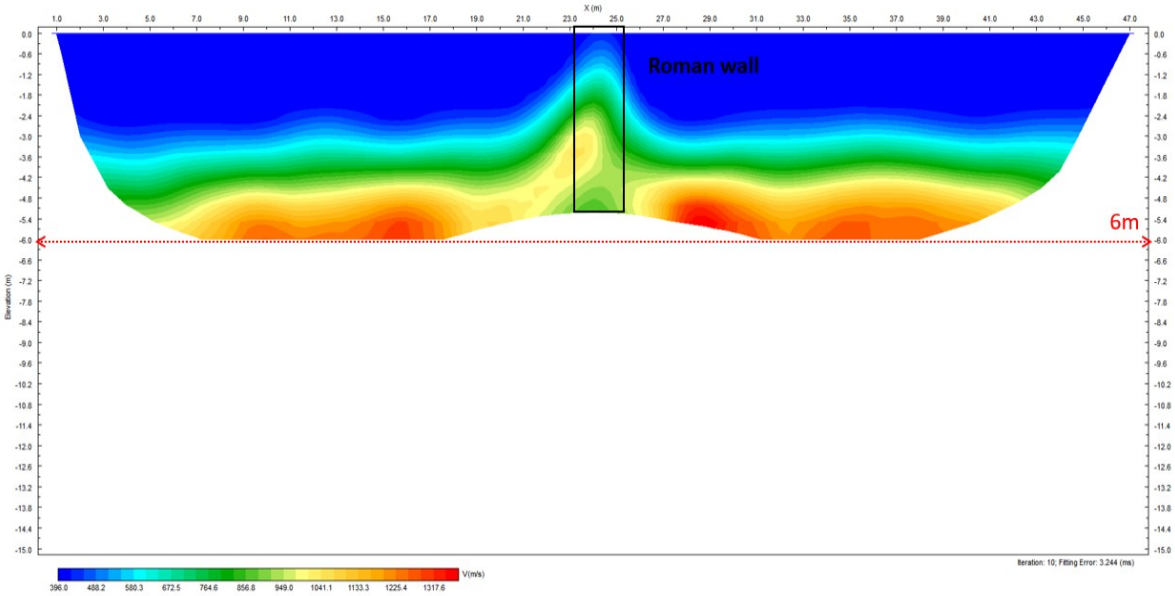

Figure 52: Inverted model for field data without ray-path

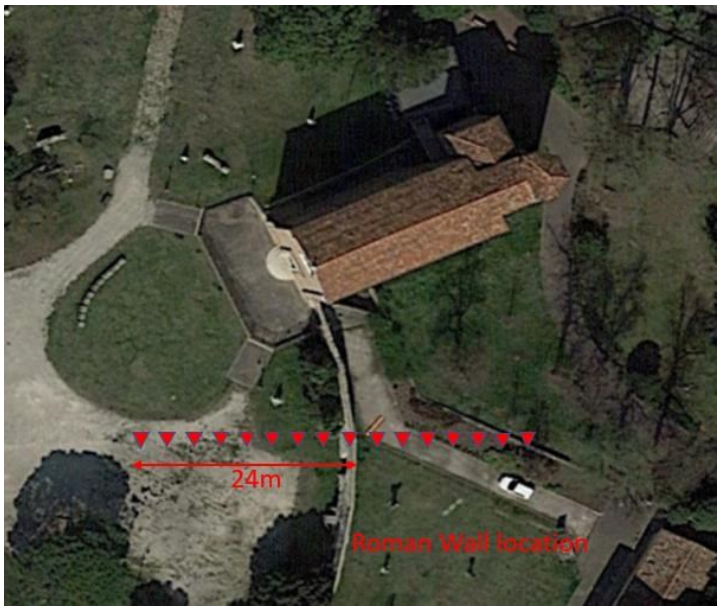

Figure 53: First horizontal line location and Roman Wall position

5.2 3D Refraction Tomography

Figure 54 shows the 3D refraction tomography on the surface with few distinct features such as two Roman walls, a low velocity zone and the Scrovegni Chapel. The survey area on the boundary in the far West-East direction exhibits a high velocity on the surface which remain uncertain. Nonetheless, further analysis and exploration are required to clarify the characteristics of this area. The walls exhibit a high velocity range of 1000 to 1500 m/s, while the low-velocity zone and the chapel both display a velocity of 400 m/s. Figure 55 displays a cross-section in the West-East direction, highlighting the presence of the wall and the low-velocity zone.

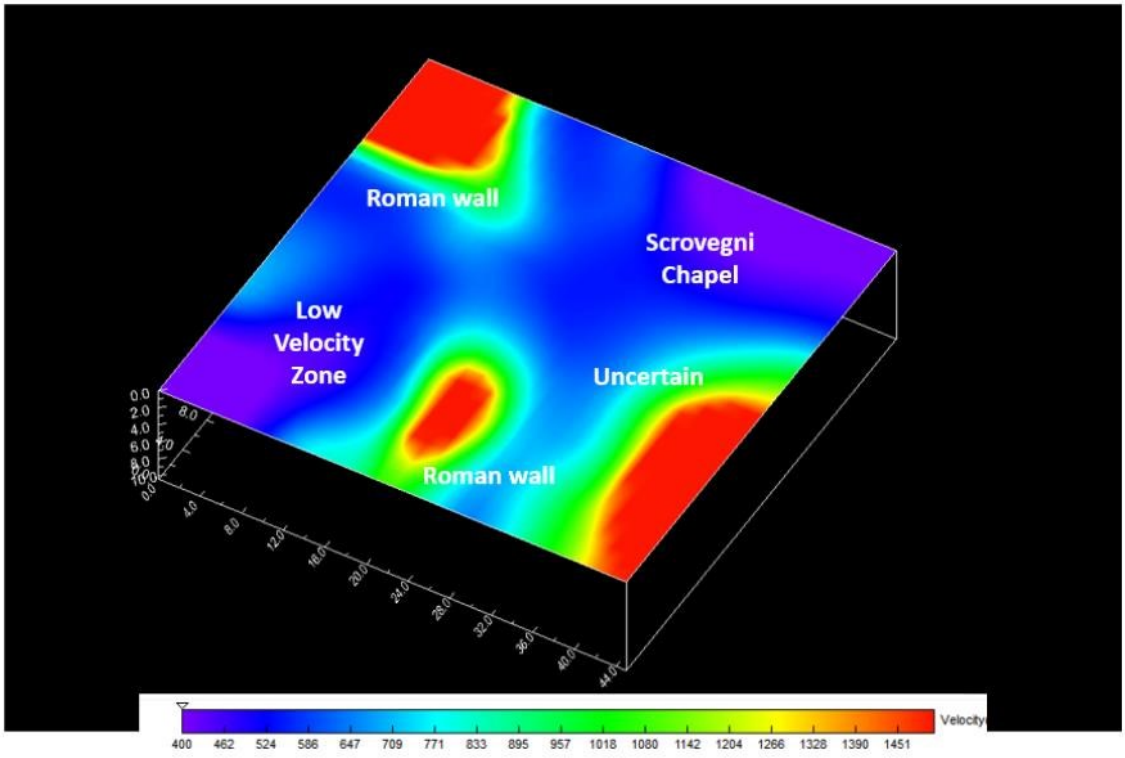

Figure 54: Inverted 3D model on the surface

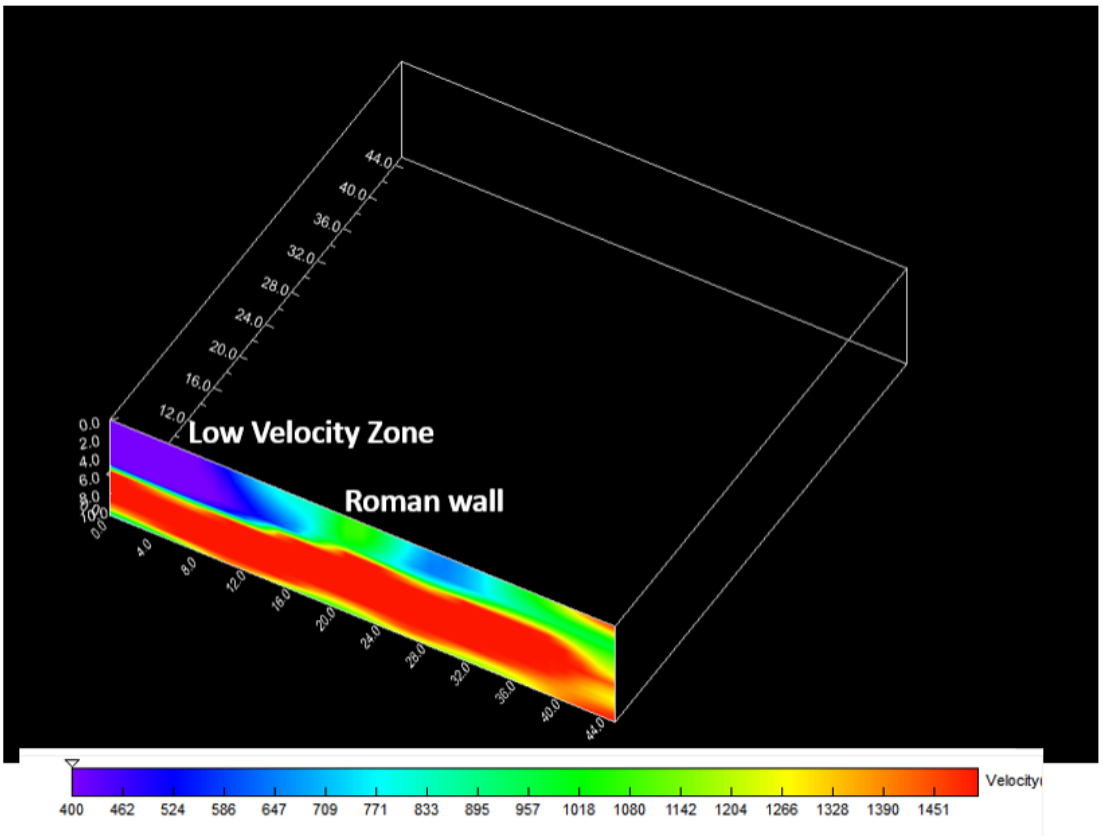

Figure 55: Cross section in East-West direction

The features continue to become visible at a depth of 2m with the same velocity, as illustrated in Figure 56.

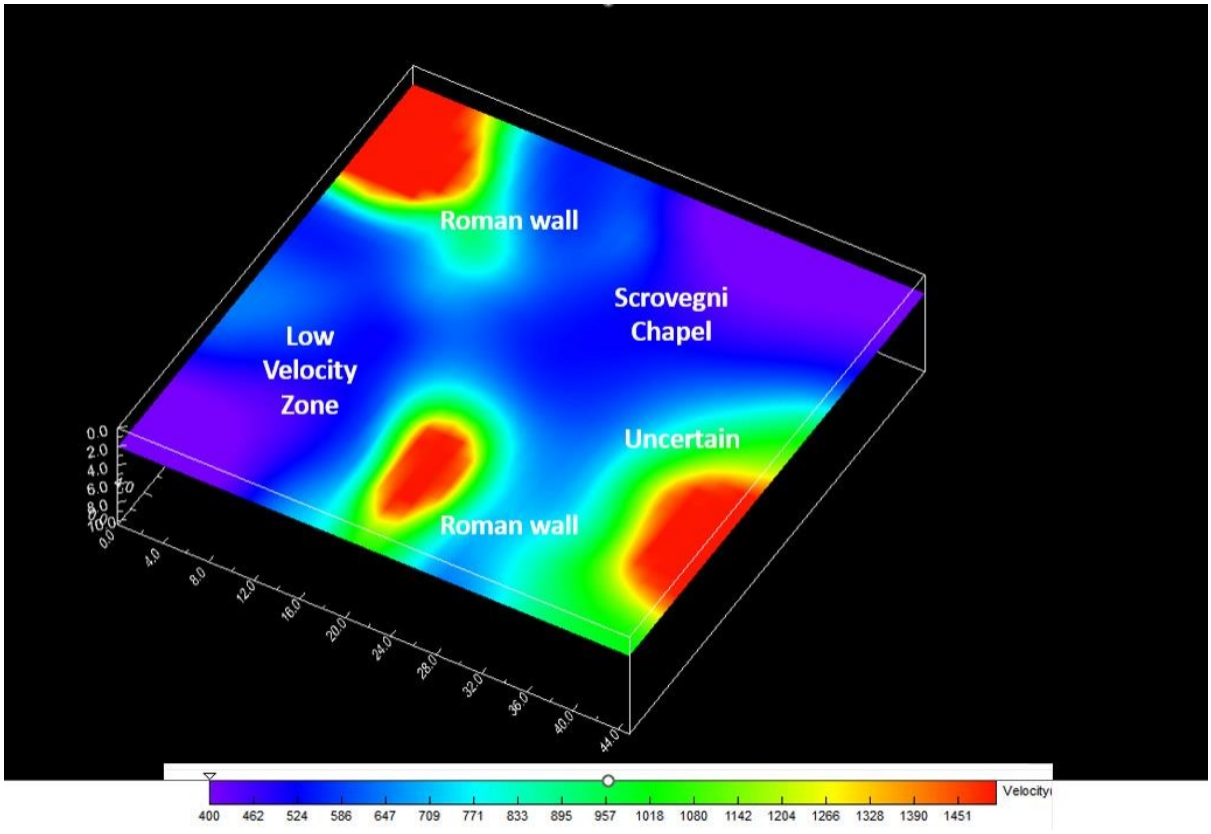

Figure 56: Inverted 3D model at 2m depth

At a depth of 4m, the wall in the West-East direction becomes slightly unrecognizable, while the wall in the South-East direction and the low-velocity zone remain recognizable as illustrated in Figure 57. It is worth noting that the velocity of the area at the chapel changes from a range of 400 at a depth of 2m to 500m/s at the depth of 4m, indicating a change in features, most likely the presence of the creek inside the chapel.

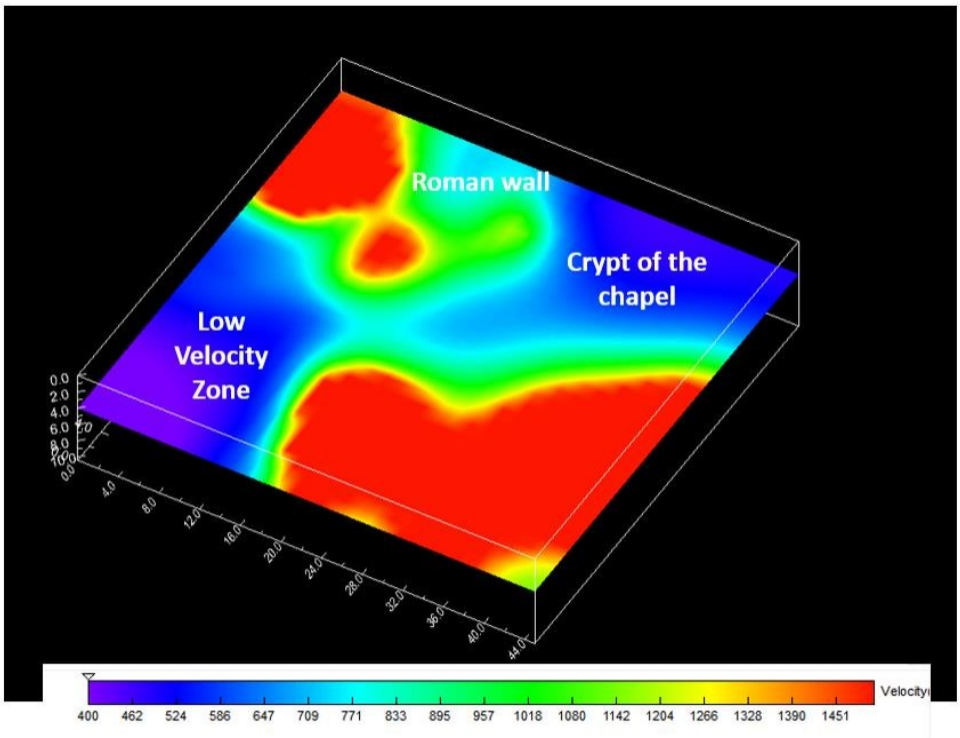

Figure 57: Inverted 3D model in 4m depth

At a depth of 6m, most of the features disappear, with only the Scrovegni Chapel remaining visible as illustrated in Figure 58. The velocity of the mostly homogeneous area ranges from 1260 to 1500 m/s, indicating the presence of the aquifer layer at this depth. The inverted 3D model consistently shows the depth of the aquifer layer at the depth of 6m, aligning with the findings of the 2D inverted model (5m to 6m)

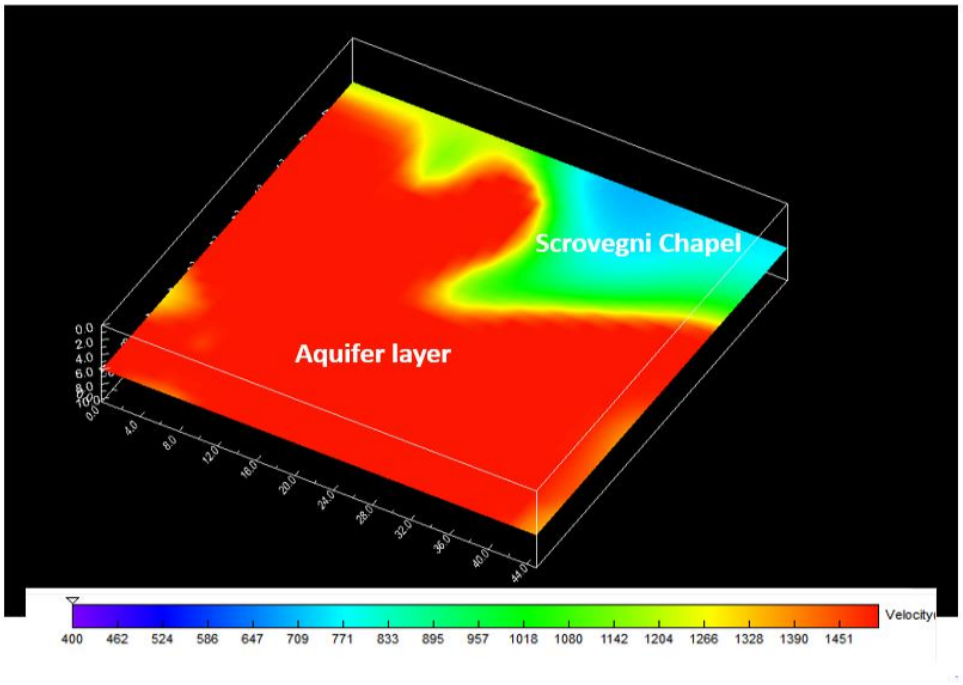

Figure 58: 3D inverted model at 6m depth

At a depth of 8m, all the features become invisible, showing a homogeneous layer with a velocity range of 1000 to 1500 m/s as shown in Figure 59.

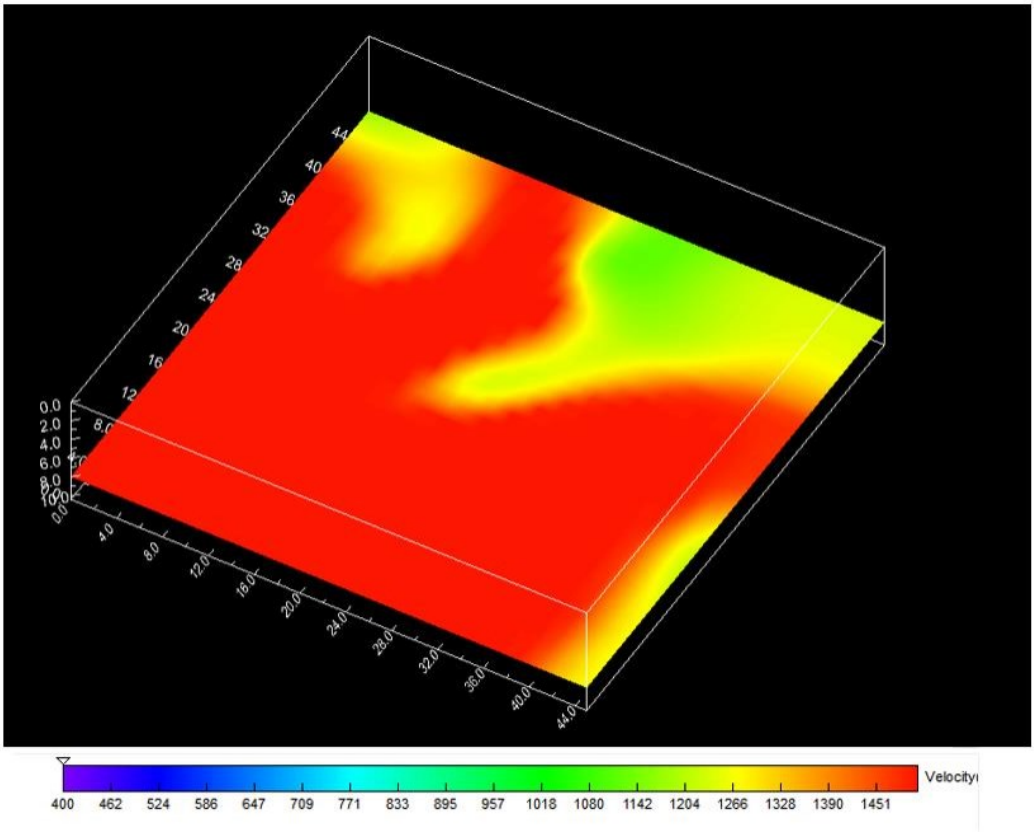

Figure 59: Inverted 3D model at 8m depth

5.3 Surface wave analysis

The examination of surface wave gradient amplitude yields auto-spectral density maps across all frequencies meanwhile the analysis of surface wave phases concludes in the extraction of phase velocity. The resulting figures describe the auto-spectrum gradient maps, phase velocity maps, standard deviation of the phase velocity and the number of measurements for each frequency. It is noteworthy that the regions near the border exhibit higher average standard deviation (error) due to the limited data coverage in these areas. The maximum error is 50 m/s, but the average error falls within the range of 10 to 20 m/s. These outcomes are reasonable given the relatively small number of shots and receivers factored into the average. Moreover, the standard deviation is inversely correlated with the number of shots; generally decreasing as the number of shots increases. The depth of penetration is also provided in relation to the corresponding frequency. The frequency range from 10Hz to 21.43Hz exhibits a very low auto-spectrum gradient on the far North-West corner, with a high phase velocity indicating the presence of the wall and some remaining Roman structures from World War II in that location. In contrast, the near South-West region exhibits a high auto-spectrum gradient and low phase velocity, indicating an amplification zone. Furthermore, in the region of the West-East direction around 24m, another high phase velocity region is found, which is consistent with the location of another Roman wall.

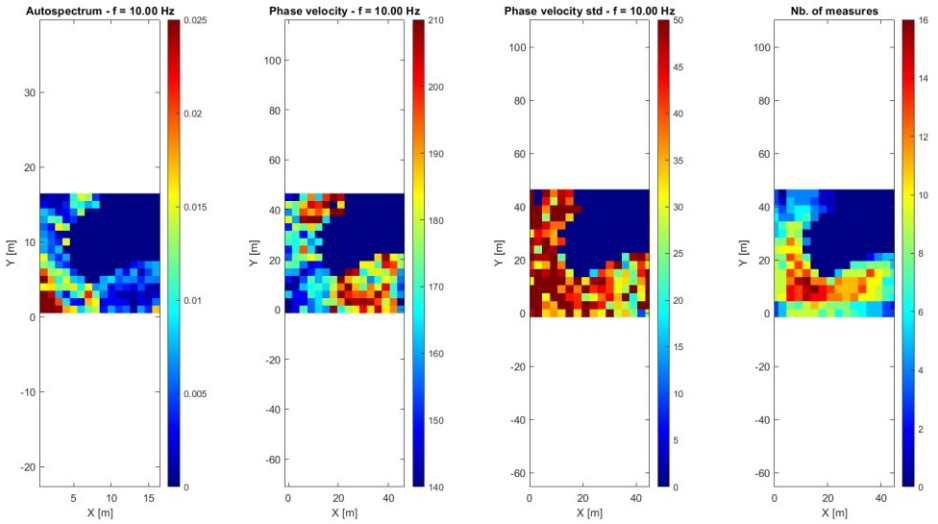

Figure 60: Results for frequency = 10Hz and maximum depth of penetration = 7.2618m

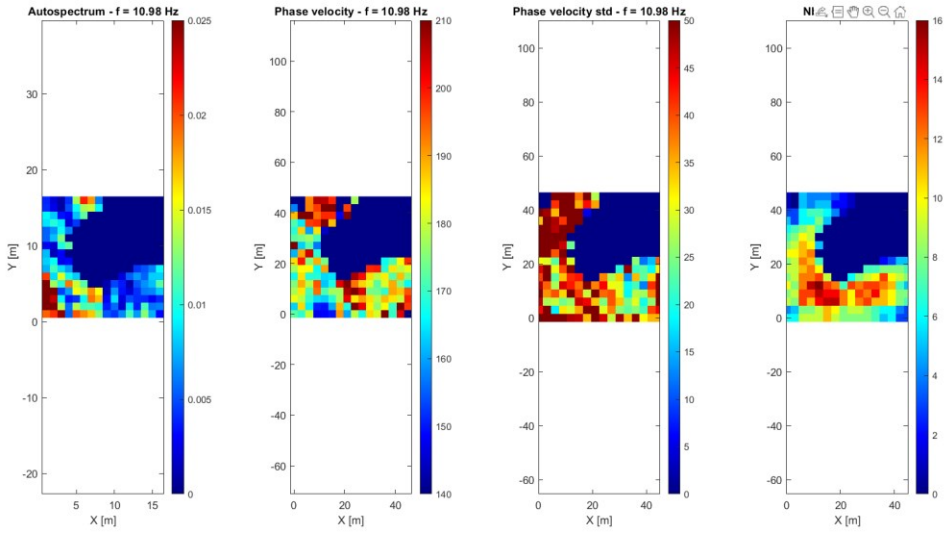

Figure 61: Results for frequency = 10.98Hz and maximum depth of penetration = 6.5983m

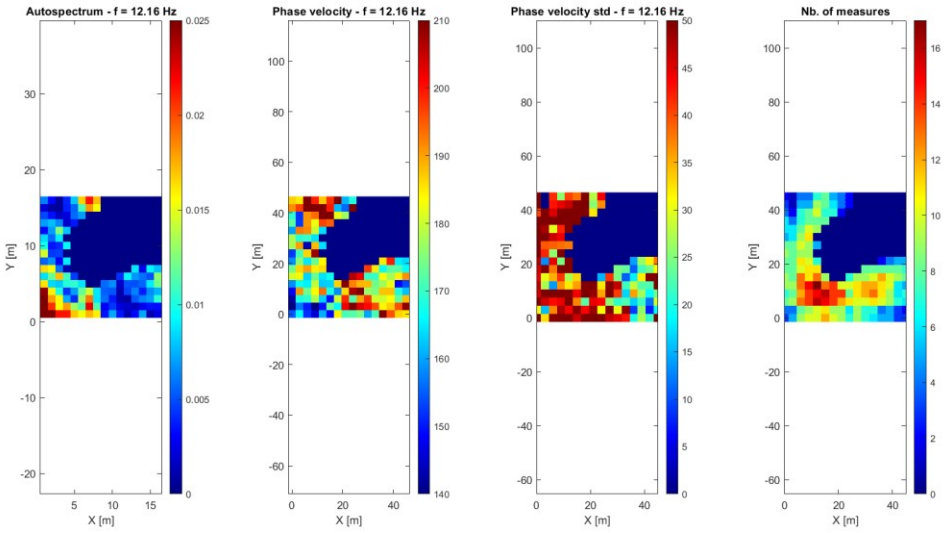

Figure 62: Results for frequency = 12.16Hz and maximum depth of penetration = 5.9648m

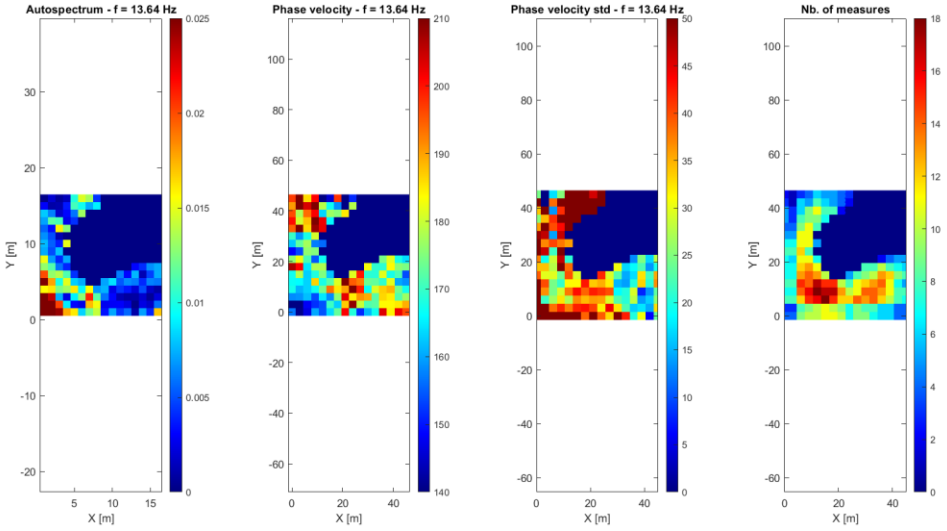

Figure 63: Results for frequency = 13.64Hz and maximum depth of penetration = 5.1794m

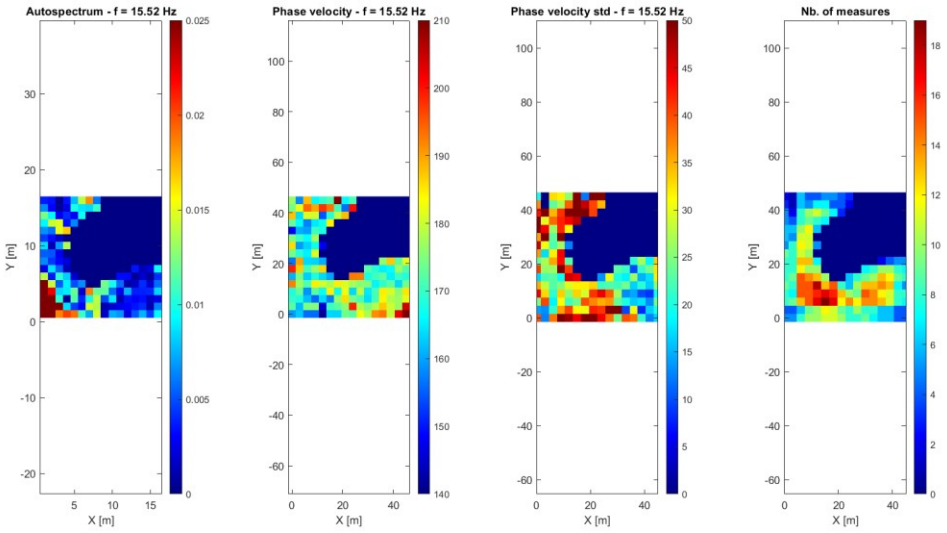

Figure 64: Results for frequency = 15.52Hz and maximum depth of penetration = 4.5152m

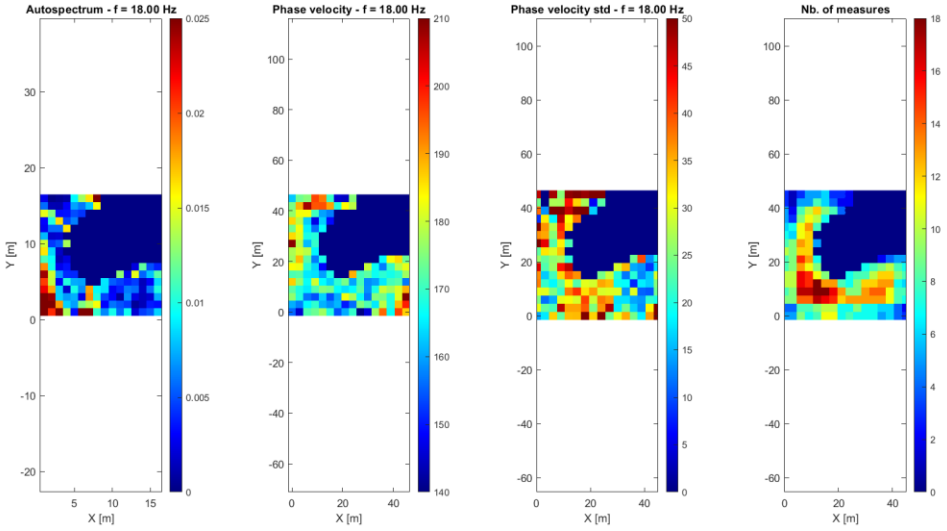

Figure 65: Results for frequency = 18Hz and maximum depth of penetration = 3.7818m

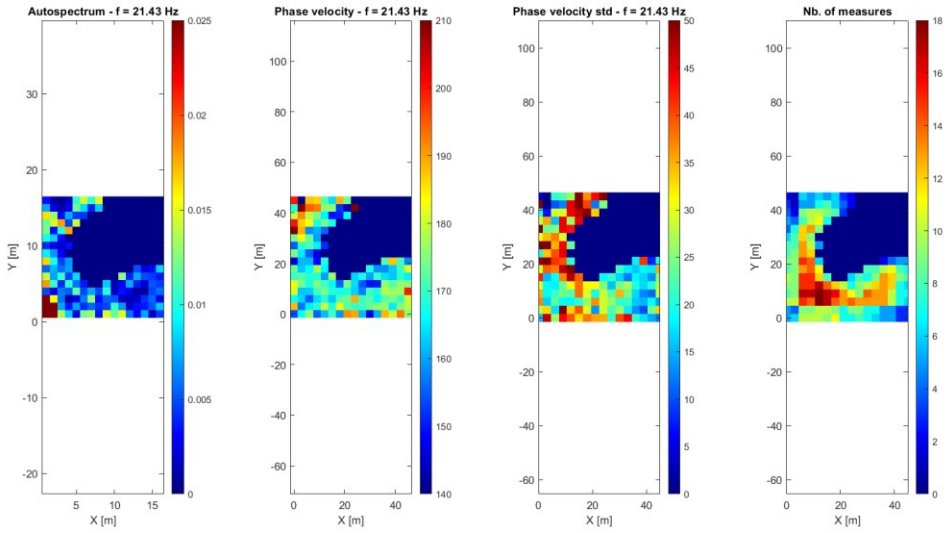

Figure 66: Results for frequency = 21.43Hz and maximum depth of penetration = 3.1734m

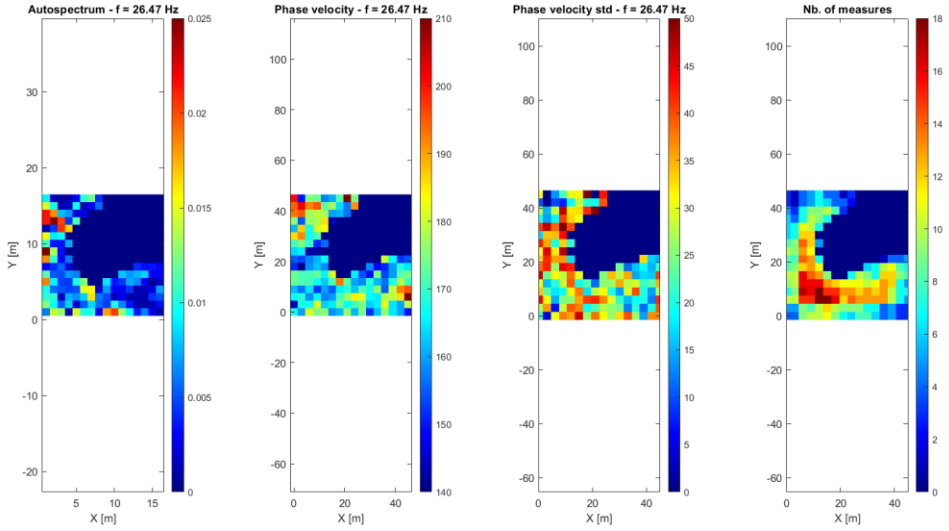

Figure 67: Results for frequency = 26.47Hz and maximum depth of penetration = 2.5503m

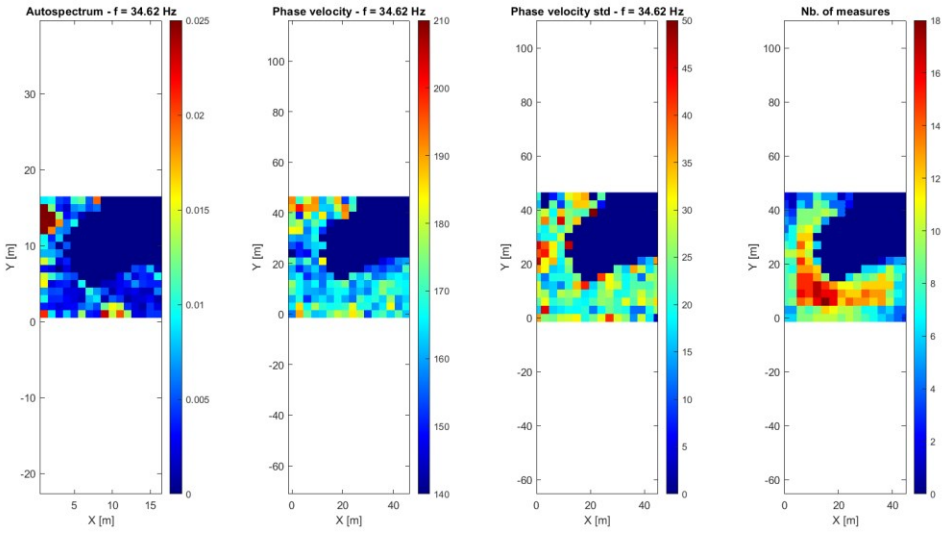

Figure 68: Results for frequency = 34.62Hz and maximum depth of penetration = 1.9211m

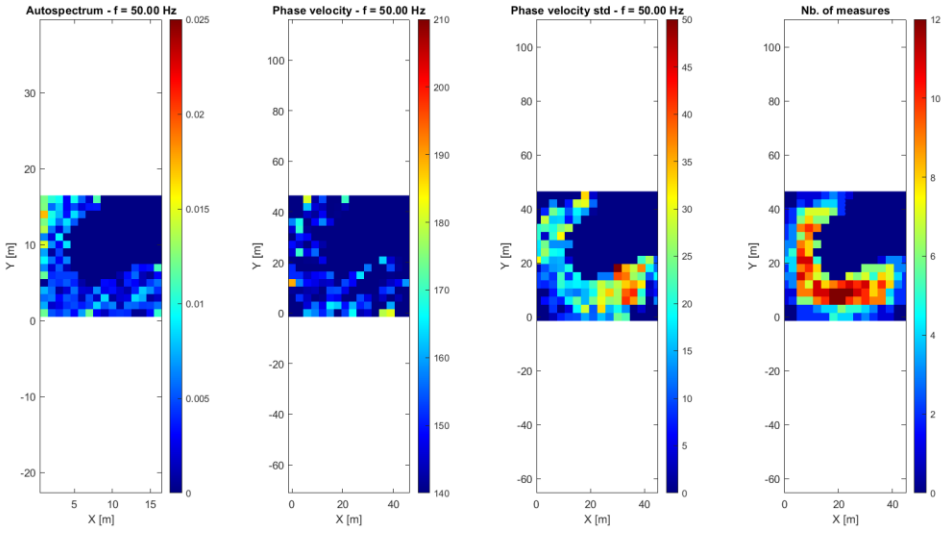

Figure 69: Results for frequency = 50Hz and maximum depth of penetration = 1.1576m

6. Discussion

A corresponding relationship between phase velocity maps and auto-spectrum gradient maps is observed at most frequencies, such that low phase velocity is commonly associated with high auto-spectrum gradient, and vice versa. However, some of the observed features are only visible at certain frequencies, mostly due to the depth of penetration and the complexity of the information obtained by phase velocity (smooth velocity variations) and amplitude (sharp lateral variations). For this reason, 3D refraction tomography is carried out in correspondence with the surface wave analysis for a clearer interpretation. The 3D refraction tomography enable the retrieval of Vp model meanwhile the surface wave analysis provide phase velocity map which is sensitive to Vs. Even though both analysis provide different information but the results shown the similar features. Figures 70 and 71 illustrate the phase velocity map and auto-spectrum gradient map with a frequency of 13.64 Hz and a maximum depth of penetration of 5.1794 m. Both figures reveal similar features, including the presence of a Roman wall and remaining structures from World War II in the far region of the South-North direction. Additionally, an amplification zone (low velocity zone) is observed in the near region of the South-North direction, along with another Roman wall in the West-East direction.

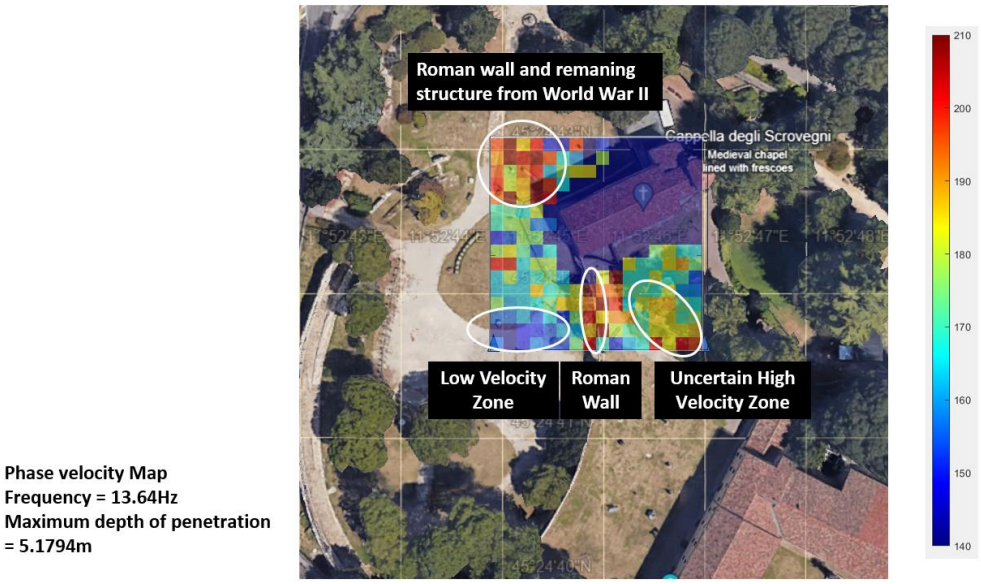

Figure 70: Phase velocity map for frequency of 13.64Hz

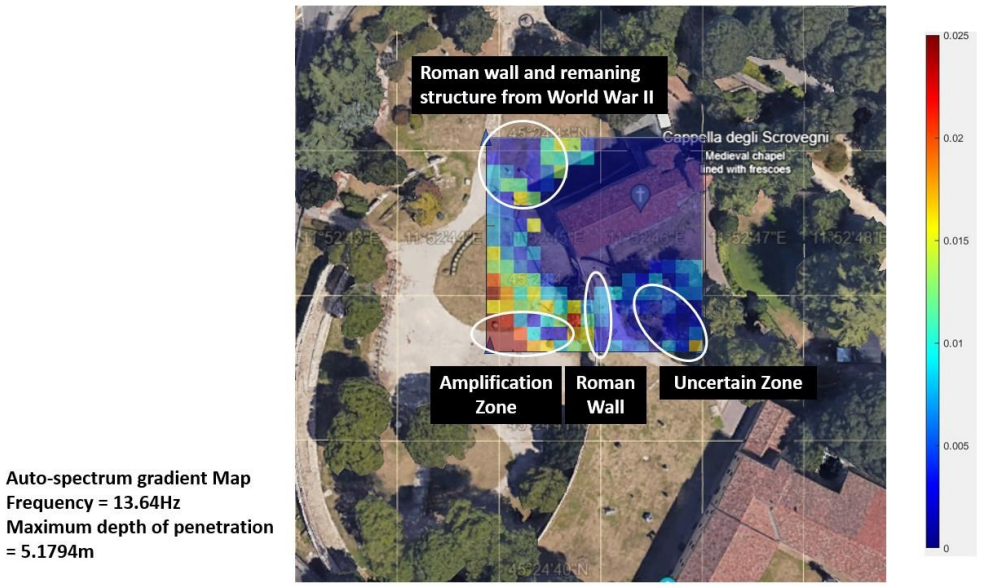

Figure 71: Auto-spectrum gradient map for frequency of 13.64Hz

The 3D refraction tomography exhibits similar features to the surface wave analysis, as illustrated in Figure 72. The Roman walls, the remaining structures from World War II, the low-velocity zone, and the Scrovegni Chapel are consistent with the surface wave analysis.

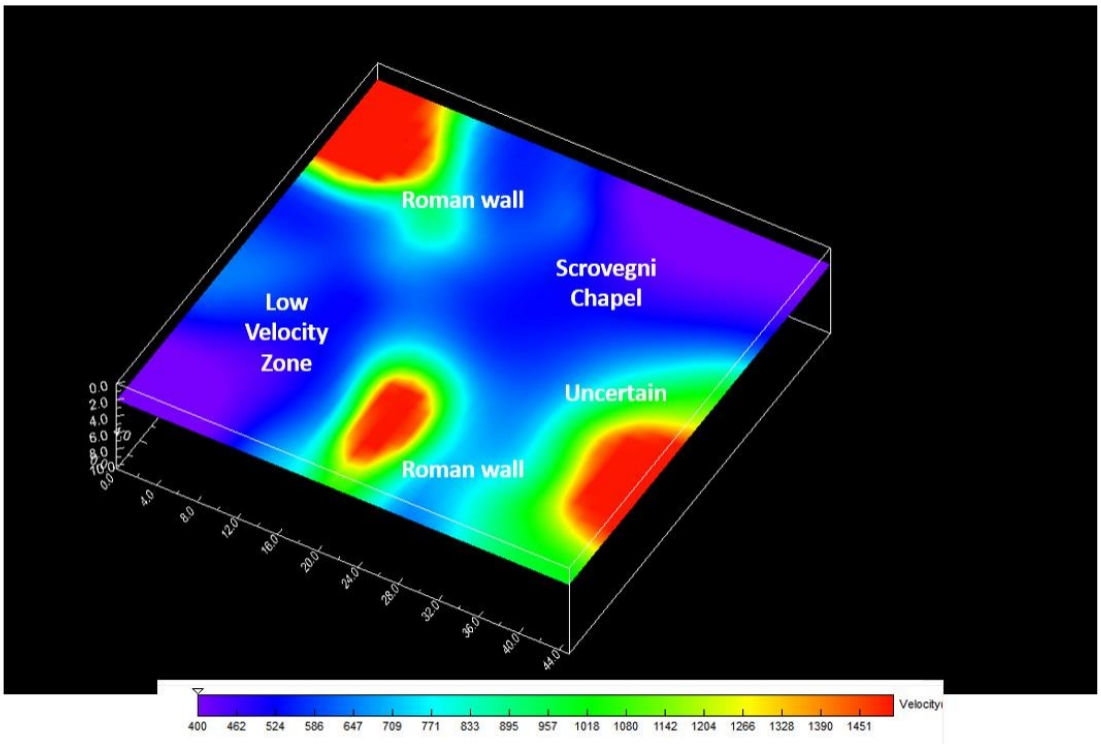

Figure 72: 3D inverted model at 2m depth

Known archaeological features, such as the Roman walls and the remaining structures from World War II, were clearly imaged, exhibiting high phase velocity and low auto-spectrum gradient in surface wave analysis, and very high velocity in 3D refraction tomography. Additionally, the observed low-velocity zone is consistent with findings from previous studies by Barone et al. (2022). The presence of this low-velocity zone within the amphitheatre challenges its attribution to a structural feature due to its size and position (Barone et al., 2022). Nevertheless, an uncertain region is identified in both the

3D refraction tomography and the surface wave analysis, exhibiting a high velocity in the phase velocity map and 3D refraction tomography, along with a low auto-spectrum gradient in the auto-spectrum gradient map. This area presents an opportunity for further exploration to uncover potential remaining buried structures.

These results emphasize the effectiveness of combining 3D refraction tomography and surface wave analysis in successfully detecting small-sized shallow velocity anomalies for further shallow survey applications.

7.0 Conclusion

The combined analysis of 3D refraction tomography and seismic surface wave analysis demonstrates its value of conducting shallow seismic surveys with a dense 3D dataset. The survey used 188 nodes and 28 active shots, with data processed for both 3D refraction tomography and surface wave analysis. In the 3D refraction tomography results, the final 3D Vp model reveals distinct features, including two Roman walls, buried remnants of World War II structures, and an undefined high-velocity zone. In surface wave analysis, the phase velocity map and auto-spectrum maps also highlight these features even though giving different information (Vs) from 3D refraction tomography (Vp). This thesis underscores that, with appropriate acquisition methods, the integrated analysis of 3D refraction tomography and surface wave analysis offers valuable insights for archaeological purposes and shallow surveys.

References

Bruno, P.P.G. (2023) ‘Seismic Exploration Methods for Structural Studies and for Active Fault Characterization: A Review.’ *Appl. Sci.* 13(16), 9473. doi: 10.3390/app13169473.

Barone, I., Cassiani, G., Ourabah, A., Boaga, J., Pavoni, M. and Deiana, R. (2023) ‘Integrating controlled-source and ambient noise seismic measures for archaeological prospection: the Scrovegni Chapel case.’ *Geophys. J. Int* 232, pp. 1944–1956. doi: 10.1093/gji/ggac432

Zhang, X., Zheng, Y. and Curtis, A. (2023). ‘Surface wave dispersion inversion using an energy likelihood function.’ *Geophys. J. Int* 232(1), pp. 523-536. doi: 10.1093/gji/ggac331.

Barone, I., Cassiani, G., Ourabah, A., Boaga, J., Pavoni, M. and Deiana, R. (2022) ‘Surface wave tomography using dense 3D data around the Scrovegni Chapel in Padua, Italy.’ *Sci Rep*. 12, 11806. doi: 10.1038/s41598-022-16061-1.

Schwardt, M., Pilger, C., Gaebler, P., Hupe, P. and Ceranna, L. (2022) ‘ Natural and Anthropogenic Sources of Seismic, Hydroacoustic, and Infrasonic Waves: Waveforms and Spectral Characteristics (and Their Applicability for Sensor Calibration).’ Surv Geophys 43(5), pp. 1265-1361. doi: 10.1007/s10712-022-09713-4.

Fjær, E., Holt, R. M., Horsrud, P., Raaen, A. M. and Risnes, R. (2021) ‘Elastic wave propagation in rocks.’ Developments in Petroleum Science. Elsevier, 72, pp. 259-318. doi: 10.1016/B978-0-12-822195-2.00014-0

Mickus, K. (2021) ‘Pollution Assessment for Sustainable Practices in Applied Sciences and Engineering.’ Butterworth-Heinemann, 5, pp. 199-287.

Bison, P., Bortolin, A., Cadelano, G., Ferrarini, G., Peron, F., Romagnoni, P. and Stevan, A. (2019) ‘Indoor monitoring of Scrovegni Chapel Crypt.’ *E3S Web of Conferences.* 111, 02075. doi: 10.1051/e3sconf/201911102075.

Rücker, C., Günther, T. and Wagner, F.M. (2017) 'pyGIMLi: An open-source library for modelling and inversion in geophysics.' Computers & Geosciences 109, pp. 106-123. doi: 10.1016/j.cageo.2017.07.011.

Hayes, G.P., Myers, E.K., Dewey, J.W., Briggs, R.W., Earle, P.S., Benz, H.M., Smoczyk, G.M., Flamme, H.E., Barnhart, W.D., Gold, R.D. and Furlong, K.P. (2017) 'Tectonic summaries of magnitude 7 and greater earthquakes from 2000 to 2015.' Geological Survey Open-File Report 2016, 1192, pp. 148. doi: 10.3133/ofr20161192.

Hellman, K., Ronczka, M., Günther, T., Wennermark, M., Rücker, C. and Dahlin, T. (2017) 'Structurally coupled inversion of ERT and refraction seismic data combined with cluster-based model integration.' *Geophys. J. Int*. 143, pp. 169-181. doi: 10.1016/j.jappgeo.2017.06.008.

Yin, X.F., Xia, J.H., Shen, C. and Xu, H.R. (2014) 'Comparative analysis on penetrating depth of high-frequency Rayleigh and Love waves.' *Geophys. J. Int* 111, pp. 86-94. doi: 10.1016/j.jappgeo.2014.09.022.

Tosi, P., Sbarra, P. and Rubeis, V.D. (2012) 'Earthquake sound perception.' Geophysical Research Letters 39(24). doi: 10.1029/2012GL054382.

Bormann, P., Engdahl, B. and Kind, R. (2012) 'Seismic Wave propagation and Earth Models.' In: Bormann, P. (Ed.), New Manual of Seismological Observatory Practice 2 (NMSOP2), Potsdam : Deutsches GeoForschungsZentrum GFZ, pp. 1-105. doi: 10.2312/GFZ.NMSOP-2_ch2

Saleh, S.M.M. (2011) 'Body Waves.' In: Gupta, H.K. (eds) Encyclopedia of Solid Earth Geophysics. Encyclopedia of Earth Sciences Series. Springer, Dordrecht. doi: 10.1007/978-90-481-8702-7_140.

Lin, F.C., Ritzwoller, M.H. and Snieder, R. (2009) 'Eikonal tomography: surface wave tomography by phase front tracking across a regional broad-band seismic array.' *Geophys. J. Int*. 177, pp. 1091-1110. doi: 10.1111/j.1365-246X.2009.04105.

Foti, S., Lancellotta, R., Sambuelli, L. And Socco, L.V. (2000) 'Notes on *fk* analysis of surface waves.' Annali Di Geofisica 43(6).

Novotny, O. (1999) 'Seismic surface waves.' Instituto de Geociencias, Lecture notes for post-graduate studies.

Sheriff, R.E. (1996) 'Understanding the Fresnel Zone.' Geophysical corner, AAPG Geophysical Integration Committee.

Abe, S., Kobayashi, Y. and Ikawa, T. (1990) 'Seismic characteristics of the Weight-Dropping Source.' *J. Phys. Earth* 38, pp. 189-212.

Pant, D.R. and Greenhalgh, S.A. (1989) 'Lateral Resolution in Seismic Reflection'. *Geophys. J. Int* 97, pp. 187-198. doi: 10.1111/j.1365-246X.1989.tb00495.x.

Futterman, W.I. (1962) 'Dispersive body waves.' *Geophys. J. Int* 67 (13), pp. 5279-5291. doi: 10.1029/JZ067i013p05279

Acknowledgements

I extend my gratitude to Professor Barone and Professor Pavoni for their invaluable guidance and insights throughout the completion of this thesis. This work is conducted as part of the master program in Geophysics for Natural Risks and Resources at the University of Padova.